A HYBRID ANALYSIS APPROACH TO THE HIGH ENERGY STEREOSCOPIC SYSTEM PHASE II MONO-ANALYSIS

A THESIS SUBMITTED IN PARTIAL FULFILLMENT

OF THE REQUIREMENTS FOR THE DEGREE OF

MASTER OF SCIENCE IN PHYSICS

OF

THE UNIVERSITY OF NAMIBIA

BY

JIMMY NDAWEDAPO SHAFOIXUNA SHAPOPI

(201401519)

APRIL 2020

Main-Supervisor: Dr Michael Backes
(Department of Physics, University of Namibia)

Co-Supervisor: Prof. Nukri Komin
(Centre for Astrophysics, University of Witwatersrand)

Abstract

The High Energy Stereoscopic System (H.E.S.S.) is an array of imaging atmospheric Cherenkov telescopes located in the Khomas highlands of Namibia. Their primary purpose is to detect Cherenkov light (CL) produced by particles in extensive air showers which are produced by incident high energy particles (gamma rays or cosmic rays) on the Earth's atmosphere. The array consists of four 107 m^2 optical telescopes and a larger 614 m^2 collective surface area telescope in the center of the array. The larger telescope has the ability of detecting showers induced by lower energy gamma rays therefore, it's addition to the array meant a lower threshold for the entire array. This can be accomplished by sophisticated analysis techniques, however, the analysis techniques that have thus far been used have not increased the integral sensitivity of the array as a whole as would be expected, but perform worse than the standard analysis technique at medium and high energies. Data taken by the H.E.S.S. telescopes is analyzed by fitting parameterized shower model images to actual images produced when observing a source, (Model++ Analysis) using a goodness of fit approach. This work explores the distribution of a shower parameter introduced in 2009, the depth of first interaction. Adjustments to the primary depth selection criteria to distinguish signal against noise are made and applied for a more sensitive result. Multi-wavelength lag studies from Cygnus X-3 are also presented. Light curve correlations between hard/soft X-rays versus radio emissions over long periods are studied. These studies are layed out as supporting suggestions that, lowering energy threshold while maintaining integral sensitivity to those energies would assist in the study of micro-quasars and possibly infer properties of quasars.

Contents

List of Figures

List of Abbreviations and Acronyms

Abbreviation	Meaning
AGN	Active Galactic Nuclei
CTA	Cherenkov Telescope Array
DAQ	Data Acquisition System
EM	Electromagnetic
EBL	Exragalactic Background light
HBL	High Frequency BL Lac
H.E.S.S.	High Energy Stereoscopic System
IACTs	Imaging Atmospheric Cherenkov Telescopes
LCT	Large Cherenkov Telescope
MJD	Modified Julian Date
NFS	Network File System
OVVs	Optically Violent Variables
PMTs	Photomultiplier Tubes
PWNe	Pulsar Wind Nebulae
ROI	Region of interest
VHE	Very High Energy
SASH	Spatial Approximation Sample Hierarchy
ISM	Inter-Stellar Medium
GRB	Gamma-Ray Burst
TD	Topological Defects
SMBH	Supermassive Black hole
QSO	Quasi-Stellar Objects
RQ (RL)	Radio Quite (Radio Loud)
NLRG (BLRG)	Narrow (Broad) Line Region Galaxy
FSRQ	Flat Spectrum Radio Quasar
XRB	X-ray Binary

Acknowledgements

Firstly I acknowledge my parents, Wilhelmina and Immanuel Shapopi, for supporting me during this time. They worked day in and day out all the years of my life to support me and continue to do so even in my young adult period. They have continually provided me with a studying friendly environment so I may produce a result to the best of my ability.

I must acknowledge Dr. Michael Backes who, through tireless efforts secured funding for my work and facilitated all of the work done in this thesis, being either directly or indirectly involved. He has my gratitude. I also acknowledge Prof. Nukri Komin who was at the heart of computational requirements for this work and in the understanding of the software implemented. I acknowledge Prof. Andrzej Zdziarski for facilitating the work on the X-ray binaries and for the funding required to do so.

A special thanks to Prof. Werner Hoffman, who funded me, my travels and tuition fees for the duration of this work. I am overwhelmingly grateful for this extremely rare opportunity.

Now I acknowledge my colleagues in the astronomy and astrophysics group in the department of Physics at the University of Namibia who have all had indirect positive impact to this thesis, in particular Lott Frans for his competitive pressure. Lastly, I give thanks to the site crew at H.E.S.S., Volker Buchholz, Albert Jahnke, Frikkie van Greunen and Tony Hanke for making working with the telescopes easy and enjoyable.

Dedication

This thesis is dedicated to Heavenly Father and Mother without whom my life would simply be meaningless. This is dedicated to understanding Their creation and ultimately understanding Them and Their love for us, Their children.

Declaration

I, Jimmy Ndawedapo Shafoixuna Shapopi, hereby declare that this study is a true reflection of my own research and that this work, or part of it has not been submitted for a degree in any other institution of higher education. No part of this research project may be reproduced, stored in any retrieval system, or transmitted in any form, or by means (e.g electronics, mechanical, photocopying, recovering, or otherwise) without the prior permission of the author, or university of Namibia in that behalf.

I, Jimmy Ndawedapo Shafoixuna Shapopi, grant the University of Namibia the right to reproduce this thesis in whole or in part, in any manner or format, which the University of Namibia may deem fit, for any person or institution requiring it for study and research; providing that the University of Namibia shall waive this right if the whole thesis has been or is being published in a manner satisfactory to the University.

Jimmy Ndawedapo Shafoixuna Shapopi  31 October 2019

Chapter 1

Introduction

The High Energy Stereoscopic System (H.E.S.S.), located in the Khomas highlands, is a system of Imaging Atmospheric Cherenkov telescopes (IACTs). These have the purpose of detecting Cherenkov radiation produced in the Earth's atmosphere by high energy particles, which are themselves produced by the interaction of an incident gamma ray with particles in the atmosphere. Phase II of the H.E.S.S. experiment pertains to the addition of a fifth Cherenkov Telescope named CT5. It has a mirror surface area of 600 m^2 and can reach threshold energies of the order of $\sim$ 10 GeV owing to the finely pixelated camera [1]. This makes CT5 a model instrument for filling the gap in the very high energy (VHE) spectrum of sources observed by phase I (CT1–4) of the H.E.S.S. experiment and the space based *Fermi* Large Area Telescope (*Fermi*-LAT).

To analyze data taken by the telescopes, filters are applied to the imaged events to remove background events one of which is a minimum telescope triggering filter, which requires more than one telescope to have been triggered by the event. However, another method exists of analyzing the "special" data taken by the larger telescope CT5. This analysis method is called the mono-analysis which attempts to reconstruct events detected by only CT5. Efforts have been made to combine this analysis method with the standard method [2]. The standard analysis method is that which does an analysis using stereoscopic triggers, as detailed above.

This "combined" method suffers a flaw, in which it does not perform, at least, as well as the standard method at medium to high energies [2]. This thesis explores one avenue of increasing the sensitivity of the mono-analysis embedded in the combined analysis, by optimizing the cuts applied to the depth of first interaction separation variable, and possible applications of a better analysis. The thesis is structured as follows:

Chapter 1 introduces the High Energy Stereoscopic System and the different methods used to analyze the data.

Chapter 2 gives a basic overview of multi-messenger particle astrophysics, the particles involved and a few mechanisms responsible for their acceleration. It also provides an in depth study about high energy particles, such as X-rays and gamma rays, and their origins.

Chapter 3 contains a summary of X-ray and gamma-ray astronomy today.

Chapter 4 gives an overview of the working principles of all detection instruments used in this work, with emphasis on gamma-ray detection.

Chapter 5 describes in detail the data used in this thesis, its handling and the analysis techniques used.

Chapter 6 reports the results obtained, statistical analyses and possible interpretations and implications of the results.

Chapter 7 In this chapter, conclusions based on observations are drawn and possible further research paths recommended.

Chapter 2

Multi-messenger Particle Astrophysics

The standard model of particle physics predicts the existence of a plethora of particles and many of these predicted particles have been detected and serve as messengers from distant locations in the Universe. These particles carry information crucial for understanding not only the origin but the future of the Universe. To detect, quantify and interpret the messages these particles carry, different forms of detection techniques are required depending on the interactive behavior of these cosmic messengers. These messengers include charged particles (nuclei) such as protons, and non-charged particles such as neutrinos and photons [3–6].

Figure 2.1 illustrates the paths taken by different particles. Each particle interacts in a different way with the interstellar medium (ISM) or the magnetic fields produced by inter-Stellar media and/or galactic and extra-galactic objects. Neutrinos are the only cosmic messengers that keep their exact intrinsic directional properties from the source. Photons are slightly deflected and cosmic rays completely diverted.

2.1 Cosmic Rays

Any charged particle outside the Earth's atmosphere is considered a cosmic ray (CR). In addition the particles generated from interactions of CRs with other nuclei can also be considered CRs. Cosmic Ray research has played a major role in the study of

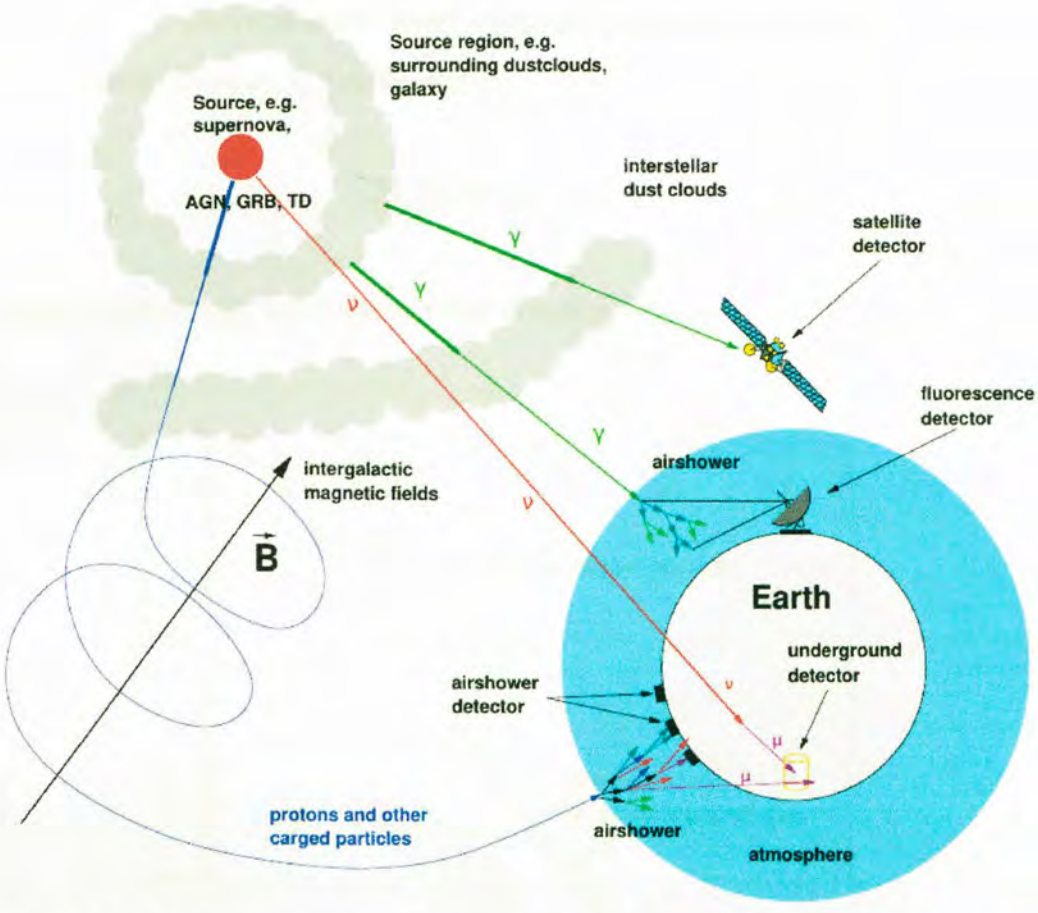

Figure 2.1: Paths traversed by cosmic messengers. Only neutrinos are absolutely unaffected by dust clouds and magnetic fields. Photons are only partially deflected by dust clouds and cosmic rays are extremely diverted by magnetic fields. Figure from [7].

elementary particles and their interactions [6]. The bulk of the cosmic ray flux incident on Earth is made up of protons ($\approx$ 85% for energies higher than $\sim$ 1 GeV [8]) traveling at high speeds, translating to high energies. The rest consist of leptons ($\approx$ 2%), mostly electrons, alpha-particles ($\approx$ 12%) and heavier nuclei up to the ferrous ion (Fe^{2+}) [5, 6, 8, 9].

As seen in Figure 2.1, CRs cannot be used for directional information. However they can be used to understand the mechanisms for particle acceleration up to ultra high energies (UHE). The CR spectrum for hadrons is shown in figure 2.2. The flux of low energy CRs is far higher than that of the highest energy ones moving from 1 $m^{-2}\,s^{-1}$

to 1 $\mathrm{km}^{-2}\,\mathrm{y}^{-1}$. Constant at the lowest energies, it softens[1] at a few GeV taking on a spectral index of about -2.7, in the form:

$$N(E)\,dE \propto E^{-2.7}\,dE \tag{2.1}$$

where E is the energy and N the number of hadrons [6].

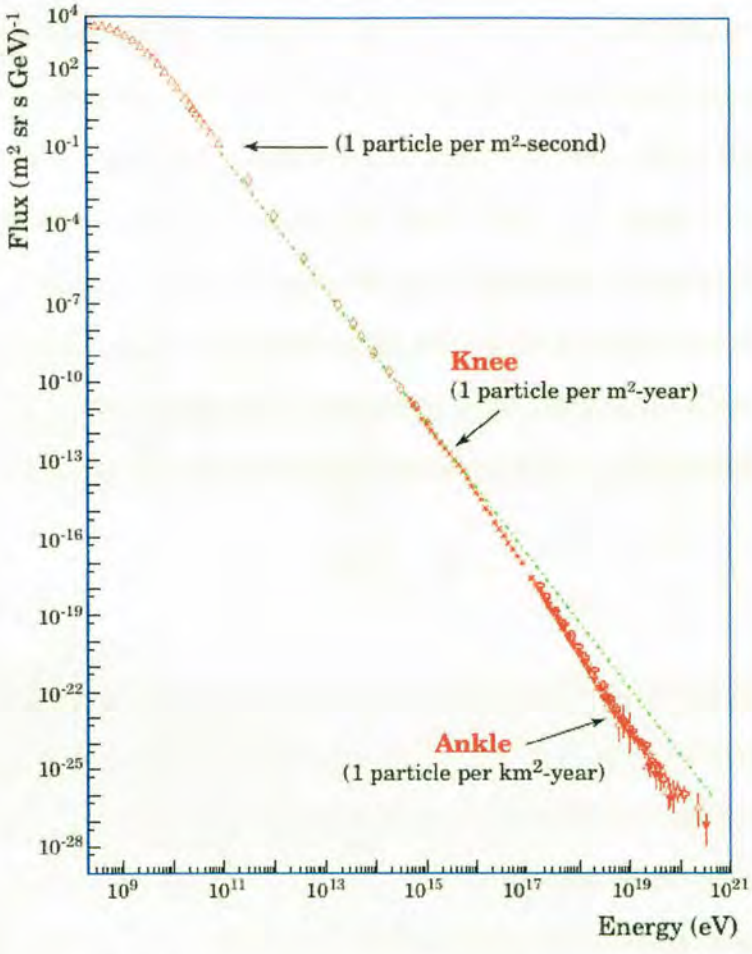

Figure 2.2: Cosmic-Rays spectrum depicting the main features, i.e. the knee and ankle at 10^{16} eV and $4 \cdot 10^{18}$ eV respectively. The flux is constant at the lowest energies and a cut off at $4 \cdot 10^{19}$ eV, called the GZK cut off, where the spectrum softens drastically can be observed, Figure from [7].

Above the so called knee ($E > 10^{15}$eV) the spectrum softens further to a spectral index of about -3.0 then hardens at the so called ankle at 10^{18}eV. The spectrum

[1] In spectral analysis softening refers to the slope of the spectrum steepening and hardening refers to the slope taking a more shallow form.

hardens continually until it reaches the GZK[2] cut off where the flux drops drastically [7].

Understanding how these particles reach such high energies, 10^{20}eV, could grant insight as to how mankind can experimentally reach such energies as well. A candidate for accelerating particles to these high energies is *shock acceleration*[3]. Type II supernova, which occur when the outer shell of a star at least $8M_{\odot}$[4] is blown off after its core collapses, are thought to be the source of *shock fronts*. These fronts, which traverse from the supernova's site at very high speeds, are a mechanism for CR acceleration in a galaxy [6]. A particle may cross this front and be backscattered by the fields of the gas traveling behind the shock front. The particle thus crosses the front again, only this time traveling in the same direction. Magnetized clouds ahead of this front could once again redirect the particle so it crosses the front again and repeat the process. Repeating this a number of times can accelerate the particle to the high energies observed in the spectrum. The energy gain is approximated by:

$$\frac{\Delta E}{E} \sim \frac{u_1}{c} \tag{2.2}$$

where u_1 is the velocity of the shock wave and c is the speed of light [6]. The energy gain is of course also dependent on the number of times the CR crosses the shock front and this needs to be taken into consideration in any calculation. Shock acceleration can account for proton energies up to two orders of magnitude below the knee and rarely higher. This can easily be understood when one takes into account the equation for the Larmor radius:

$$R_L = \frac{\gamma m v}{qB} \tag{2.3}$$

where $m = m_p = 1.67 \cdot 10^{-27}$kg, v is the velocity of the proton, q its charge, B the magnetic field in which this proton is submerged and γ is the Lorentz factor.

[2]Greisen–Zatsepin–Kuzmin

[3]Also known as Diffuse Shock Acceleration (DSA).

[4]Solar Mass

As $v \rightarrow \infty, R_L \rightarrow \infty$, thus protons of the highest energies must have very large Larmor radii. Large R_L directly translate to extra-galactic origin given that if they did have galactic origin the probability of the proton being incident on the Earth would be vanishing. The reasoning behind this is that the CR would have to leave the galaxy, as it has a R_L too large to continuously gyrate in the galaxy, and come back into the galaxy to reach earth. This seems statistically unlikely therefore it is concluded that large R_L translates to extra-galactic origin. Different mechanisms are used to explain the origins of high energy CRs, one such object is called Active Galactic Nuclei [5], explained in Subsection 2.4.

2.2 Neutrinos

Neutrinos are small (compared to photons), light and charge-less and retain their directional information because of their rare interactions with the ISM, as Figure 2.1 illustrates. Even if they come from the core of their source they are unlikely subject to scattering such as the *random walk* of photons from the center of the sun. Their small cross section means they do not easily interact with other particles making neutrinos difficult to detect [8]. The discovery of neutrinos involved indirect detection of Cherenkov light (see Subsection 3.2.1) a result of a sub-process produced by a highly energetic positron, which itself was produced by the interaction of an electron anti-neutrino ($\bar{\nu_e}$) with a proton, $p + \bar{\nu_e} \rightarrow n + e^+$ [10]. This was one of 20 anti-neutrinos detected from a supernova named 1978A in the Large Magellanic Cloud (LMC). About 99% of the energy produced in this supernova was carried off by the 6 types of neutrinos, as predicted by the standard model, $\nu_e, \bar{\nu_e}, \nu_\tau, \bar{\nu_\tau}, \nu_\mu, \bar{\nu_\mu}$ [6, 11–14].

The detection of these particles is, as mentioned above, a complicated and arduous endeavor. One technique of detecting these particles involves the construction of large underwater tanks for isolation from photons and CRs. These are developed in such a manner that any disturbances can only be caused by neutrinos [6].

2.3 Photons

Figure 2.1 depicts the behavior of photons in the cosmos. As can be seen from the figure, photons traverse straight paths keeping large amounts of their initial directional data. Some photons do not keep all their directional information as some may be deflected by particles in the ISM because, unlike neutrinos, photons have a large enough cross section for interaction.

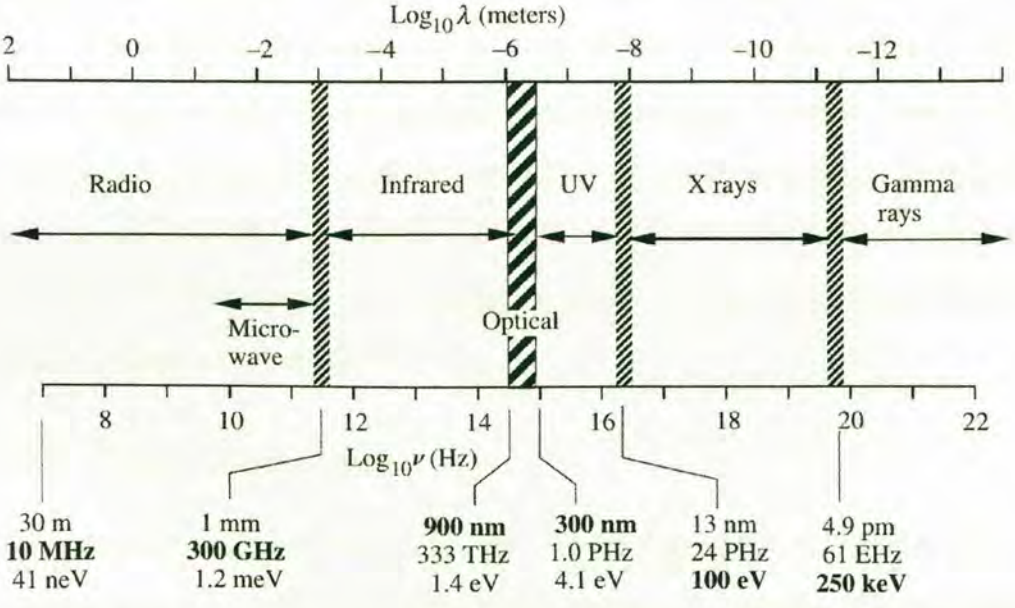

Figure 2.3: Electromagnetic spectrum depicting all classes of photons (Electromagnetic radiation) their logarithmic frequencies in Hertz and logarithmic wavelengths in meters. Also shown are their corresponding energies in electron volts, Figure from [5].

Depending on their energy, photons have different designations. The electromagnetic spectrum in Figure 2.3 shows the energies with their corresponding wavelengths and frequencies, low energy radio waves from the left to higher energy X-rays and UHE gamma rays to the right. Normal matter absorbs EM radiation. An object that absorbs all radiation falling on it, is considered to behave as an idealized, non-existent body called a blackbody. When the matter and radiation are in thermodynamic equilibrium, i.e. the blackbody is at uniform temperature, it emits photons over almost the entire

EM spectrum at different intensities. Planck's equation defines the photon flux of a blackbody for some temperature T:

$$f_\nu = \frac{2\pi h\nu^3}{c^2} \frac{1}{e^{h\nu/kT} - 1} \tag{2.4}$$

where h is Planck's constant, k Boltzmann's constant and ν the frequency [15]. Figure 2.4 shows the spectrum of a blackbody over different frequencies, which peaks at different frequencies depending on the temperature and approaches zero asymptotically at higher frequencies. Thus there is a limit to the energy of a photon emitted by a blackbody. The dark red vertical line to the right of the plots clearly shows that a blackbody cannot emit an X-ray photon at these temperatures. As the temperature gets higher the flux peaks at higher frequencies. However, from Equation 2.4 it can be seen that when temperatures get too high the flux diverges. To produce a gamma ray of 61 EHz the blackbody would need to be heated to a temperature of $1.7 \cdot 10^{19}$ K. Thus gamma rays can only be produced in non-thermal processes that will be outlined in Subsection 2.3.1.

2.3.1 X-rays & Gamma Rays

The threshold frequency for X-rays, as seen in Figure 2.3, is 24 PHz (13 nm) corresponding to $\sim$ 100 eV. As mentioned in Section 2.3, photons of higher energies than this must be produced in non-thermal processes. In practice, these processes are split into two: leptonic and hadronic.

Leptonic Processes

Leptons are elementary particles that do not take part in any strong interaction, responsible for the strong nuclear forces. They interact only with bosons such as photons [16].

Bremmstralung also known as "braking radiation", occurs when a high energy electron (in fact any charged lepton) travels near a nucleus and is deflected in the

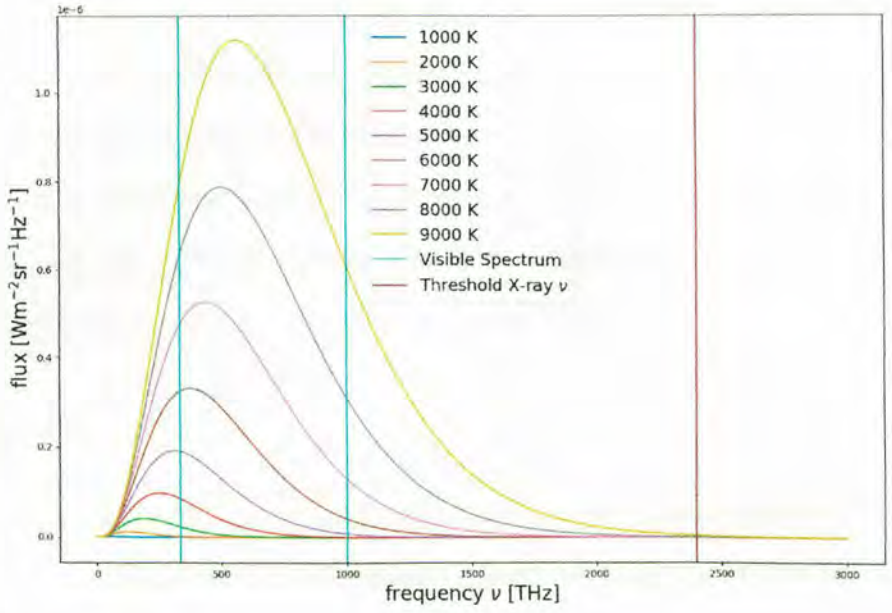

Figure 2.4: Blackbody spectrum for different temperatures. The cyan lines show the frequency range of visible light in the EM spectrum and the dark red vertical line shows the threshold frequency for X-rays. Figure produced from Equation 2.4.

electric field, causing it to emit EM radiation with an amplitude proportional to the acceleration (in fact it is a deceleration) of the electron [4]. Higher energy electrons will undergo a higher degree of deflection and thus release higher energy photons. The highest energy photons are produced with an angle of deflection approaching 180° [3, 8, 9].

Synchrotron radiaton occurs when a charged particle moves in a magnetic field perpendicular to its direction of motion. The particle experiences a continual acceleration in the form of direction alteration, i.e it traverses a helical path. In this process, the particle releases photons continuously. The higher the particle's initial energy, the higher the energy of the EM radiation. At relativistic speeds, the radiation is beamed into a cone of angle $\theta \approx m_e c^2/E$, where m_e is the mass of an electron, c is the speed of light and E the particles initial energy. This means that instead of an instantaneous frequency for the EM radiation, a continuous spectrum is observed [3, 6, 8, 9].

Inverse Compton Scattering can be understood once Compton scattering is understood. Compton scattering is the collision of a high energy photon with a low energy electron, where the photon "transfers" energy to the electron. All calculations done in this case consider the electron to be at rest. Inverse Compton scattering thus refers to the collision of a low energy photon with a highly energetic electron and the electron loses energy to the photon. This is the dominant mechanism by which VHE gamma rays are produced in astrophysical sources [4].

Hadronic Processes

In the standard model of particle physics the material universe is assumed to built from elementary constituents called quarks and leptons [6]. Hadrons are particles made of 2 or more elementary quarks and take part in the strong nuclear interaction. Hadrons are divided into two sub-groups: mesons and baryons. Mesons are an even combination of quarks bounded together by the exchange of gluons (gluons are the exchange particles responsible for the strong force between quarks), whereas baryons are a combination of an uneven number of quarks. The proton and neutron for example, are combinations of up and down quarks, thus they are baryons. Mesons are generally a combination of a quark of a particular "flavor" and an anti-quark of that "flavor" [6]. Pions or pi mesons (π) fall in the meson sub-group of hadrons. A brief overview of the standard model of particle physics describing elementary particles can be found in appendix A.

Pion decay processes release photons. There are 3 types of pions differentiated by their charge: neutral (π^0), positively charged (π^+) and negatively charged (π^-). Each of these are made of different "flavors" of quarks and anti-quarks. Pions are produced by the collision of protons with hydrogen gas, if the incident proton has a threshold kinetic energy of 290 MeV [4]. The most common interaction has the form:

$$p + H^+ \rightarrow N^+ + N + n_1(\pi^+ + \pi^-) + n_2(\pi^0) \tag{2.5}$$

where N is some baryon, H^+ a hydrogen ion, N^+ a charged baryon and n_1 and n_2 are integers [4,6]. The π zero mesons will then decay into two gamma rays ($\pi^0 \rightarrow \gamma + \gamma$), as π^0 mesons have a half life of 10 fs.

2.4 Active Galactic Nuclei

Most of the processes described in Section 2.3.1 are possible processes in Galactic sources to produce X-rays and gamma rays. Sources for gamma rays outside of the Milky Way include Active Galactic Nuclei (AGN). The simplest definition of an AGN is a galaxy with a central "engine" that outshines the combination of all the stars in it, i.e. most of the energy emitted by the galaxy originates from its center. For mankind, these luminous galaxies are the principle probes of the Universe at a large scale thus understanding them is essential to the understanding of the Universe, its origin and evolution [17]. Figure 2.5 is the model of an AGN. At the center of the AGN, like most other large galaxies, is a supermassive black hole (SMBH $> 10^6 M_\odot$ [10]) whose gravitational potential energy is thought to be the ultimate source of the AGNs luminosity [17]. Matter is pulled toward the black hole (BH) and losses angular momentum to viscous and turbulent processes forming an accretion disk around the BH that emits thermal EM radiation [17]. This glow outshines the rest of the galaxy by orders of magnitude [8]. The SMBH and accretion disk are surrounded by a torus of gas and dust obscuring the central BH. The torus supplies the accretion disk with matter. The accretion of matter onto the BH accelerates particles to relativistic velocities and thus causing high energy photons to be emitted in the form of synchrotron radiation. In and around the accretion disk are regions exhibiting broad and narrow emission lines. Two highly collimated outflows of plasma called jets are formed, it is thought, from the extraction of spin energy from the SMBH. These jets expel particles at relativistic velocities and terminate in radio lobes. They are called "radio" lobes as they emit EM radiation in the radio wave regime. [3].

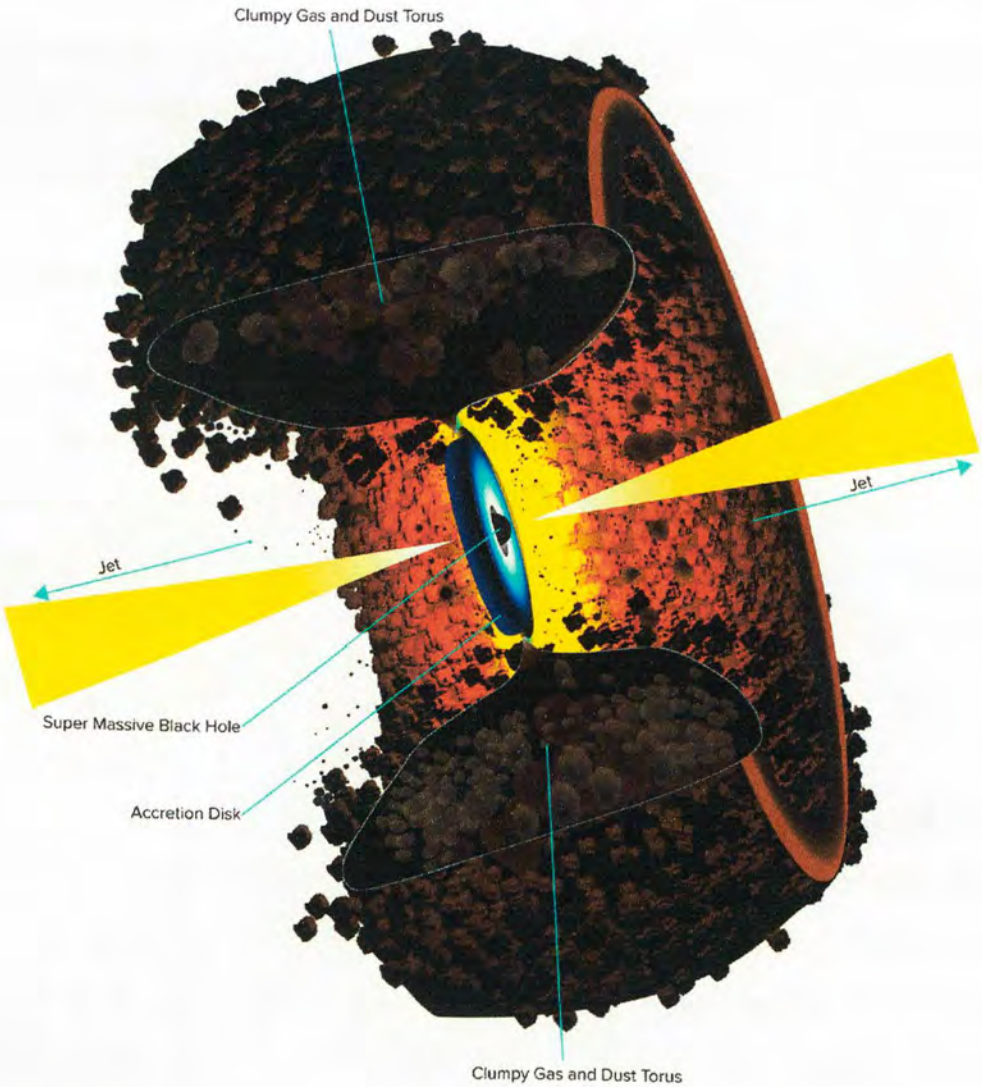

Figure 2.5: An artist's depiction of the AGN model proposed by Urray and Padovani in [17]. Figure from [18].

2.4.1 AGN Classes

AGNs are classified differently by the angle at which they are viewed. Figure 2.6 depicts the classification of AGN with their respective observational angles. Seyfert Galaxies, discovered by Carl Seyfert, are less luminous than most AGN. Most AGNs are radio quiet (RQ), i.e they emit very weak radio frequencies and are called Quasi-Stellar Objects (QSOs) [19]. About 10% of QSOs have a high radio frequency emission flux and attract attention with the collimated outflows of the jets. These QSOs are given the names Quasars or Radio Loud (RL) AGN.

2.5 Black hole X-ray binaries

Most large mass stars ($\gtrsim 16M_{\odot}$), about 80 %, are in binary or multiple systems [21]. One of the stars in an arbitrary binary system having sufficient mass ($\gtrsim 8M_{\odot}$ [10]), can evolve up to the point where neutronization[5] processes increase rapidly, reducing electron degeneracy pressure in the core of the star causing a free fall of the outer layers onto the core in a type II supernova. At this point the core will either collapse into a single point (the singularity), forming a black hole (BH), or collapse into a compact object such as a neutron star (NS).

For the binary system to remain intact the companion star must be smaller than the already collapsing star. The companion star can now lose mass to the compact object by either stellar wind accretion or Roche-lobe (RL) overflow [22, 23]. These are the two main mass transfer mechanisms that have been the subject of many studies [23–29]. In the case of stellar wind accretion, the accretion disk that may form around the BH or NS is small when compared to that formed due to Roche-lobe overflow, as the stellar winds from the massive young star lacks angular momentum. The mechanism for RL overflow involves a growing star filling up its Roche volume causing mass transfer through the inner Lagrangian point of the system to the compact object.

[5]Neutronization is a process by which a proton reacts with an electron to produce a neutron and electron neutrino.

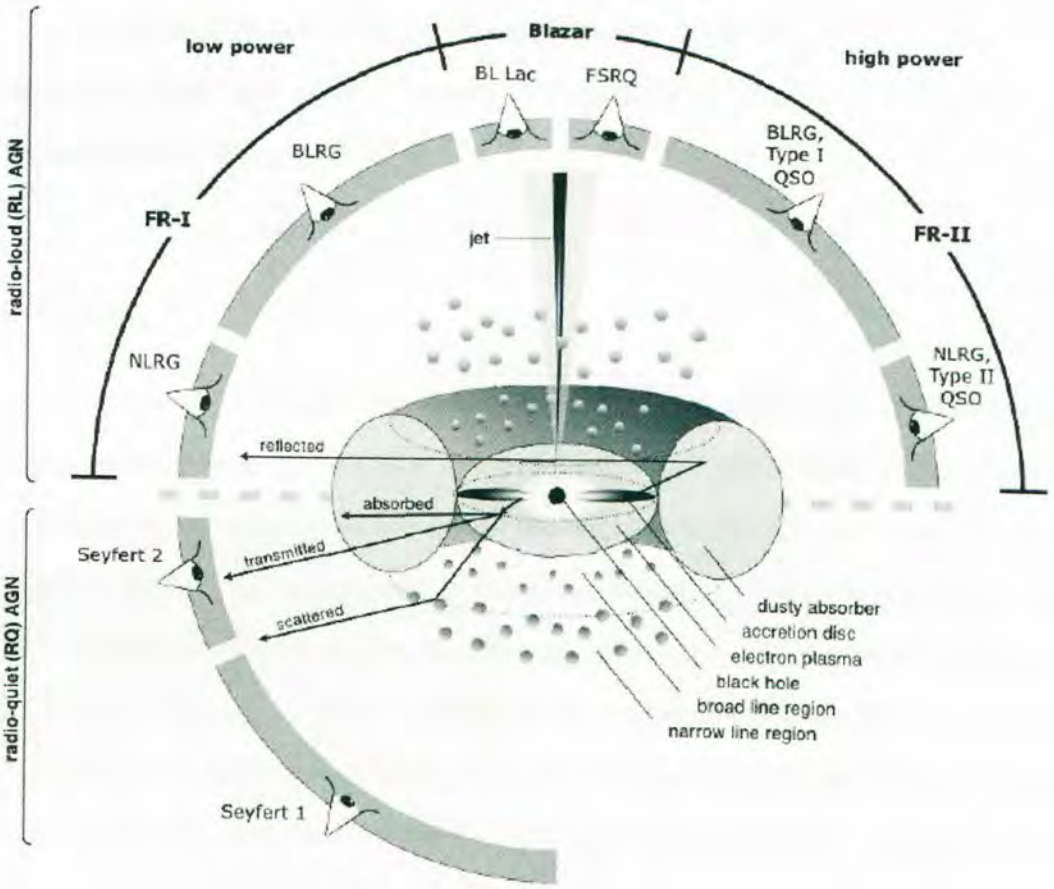

Figure 2.6: Illustration of how AGN are classified depending on the angle at which they are observed. From the line of sight below the black hole can be seen: Seyfert I (SF I) and SF II AGNs observed in the absence of a relativistic jet. In these cases the AGN is "quiet" in the radio emission. Type one Faranoff-Riley (FR I) AGN, classified as Broad and Narrow line Radio Galaxies (NLRG and BLRG). These Galaxies exhibit broad and narrow emission lines, respectively, that peak in the radio regime. Blazars, classified as BL Lacertae (BL Lac) and Flat-Spectrum Radio Quasars (FSRQ). The line of sight these galaxies is almost directly aligned with the axis of the jet. Among their differences BL Lacs have weak optical emission lines while FSRQs have very strong optical emission lines [20]. FR II galaxies are classified into Type I and Type II Quasi-Stellar Objects (QSOs) differentiated by their radio emission lines. Figure from [19].

Black hole X-ray binaries (BH-XRBs) are systems of a star and a BH (of mass $\gtrsim 20\ M_{\odot}$ [30]) in orbit of one another. These systems are similar to quasars and are thus called micro-quasars (see Figure 2.7). They are not only similar in morphology but also in the Physics that governs them. Mirabel and Rodriguez [31], suggest that there is an underlying unity in the Physics of accreting BHs over a large range of scales $[10M_{\odot} - 10^{9}M_{\odot}]$.

Cygnus X-1

Discovered in 1964, Cygnus X-1 is an X-ray binary with a black hole (BH) compact object, inferred from its cross-over of the Oppenheimer-Volkoff limit[6] [32]. This is a high mass binary system which is one of the brightest in its class and one of the best studied [33–35]. The companion of the X-ray binary is an O-type supergiant and loses mass to the BH via the RL overflow mechanism, through the inner Lagrangian point [27–29, 36, 37]. Cyg X-1 exhibits X-ray emission which has its origins most likely from the accretion disk. Radio emission are also characteristic of Cyg X-1 and is thought to be from the resolved relativistic jets ejected from the compact object. Studying the relationship between the X-ray and radio emissions from BH X-ray binaries (BHXRBs) is important to understanding the accretion of matter onto a black hole and its outflow [33].

Cyg X-1 shows two main spectral states, i.e. hard and soft. These states are distinguished by the shape of the X-ray spectra [38]. In the hard state, the spectrum exhibits a hard power law with a high energy cut-off above $\sim$ 100 keV. In this state, the disk is weak, i.e. it has lower X-ray emission when compared to the soft state. In the soft state, the spectrum adopts a high energy tail with varying strength and the disk emits a high flux of soft blackbody X-rays [38].

[6]Upper limit for the mass of a neutron star

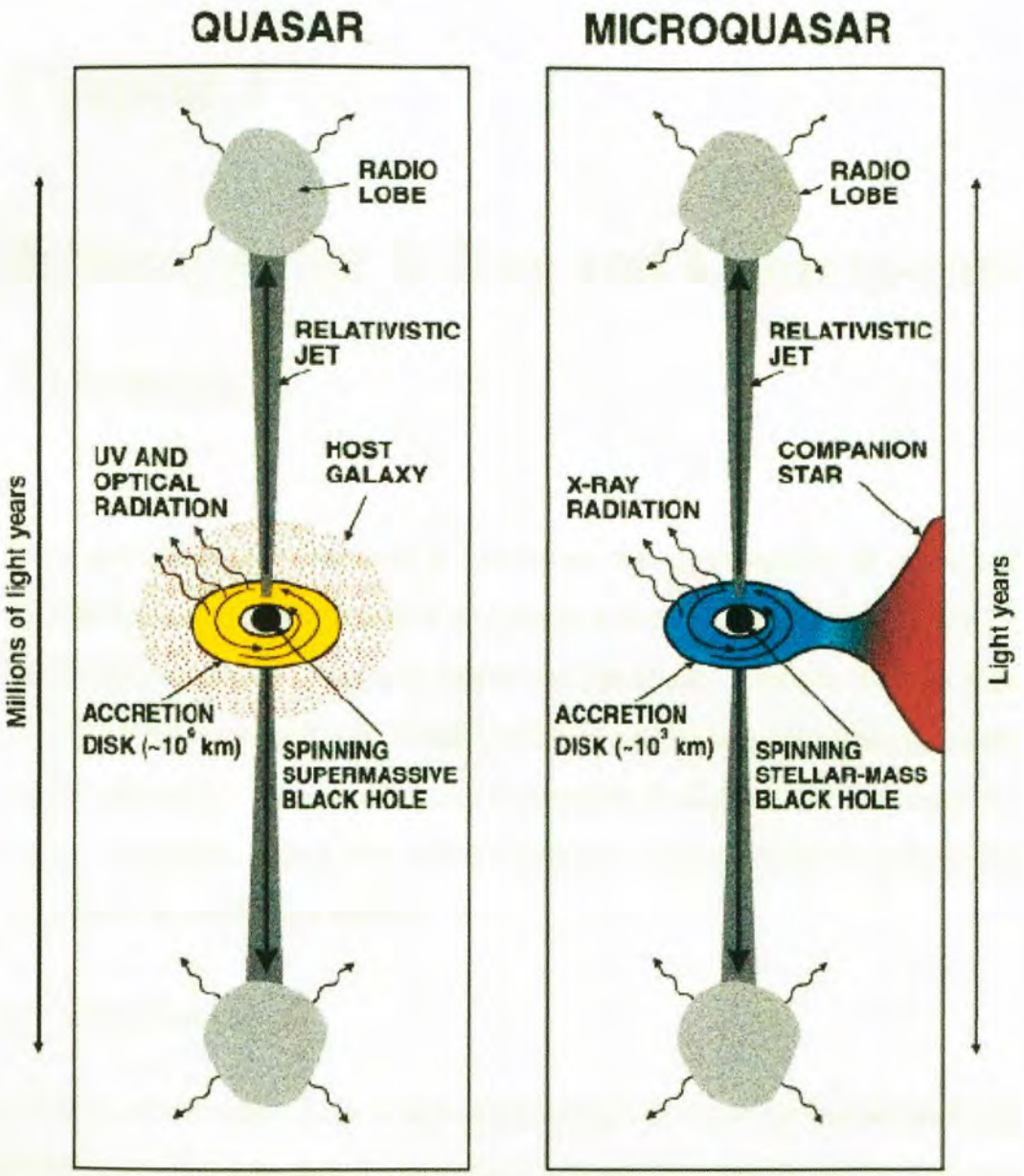

Figure 2.7: Illustration of the current ideas surrounding quasars and micro-quasars. A spinning BH accreting matter from a star (or host galaxy for quasars) emitting X-rays in the process (Quasars emit across the EM spectrum). The superluminal jets are depicted showing the extent in orders of magnitude. Figure from [31].

Chapter 3

Telescopes for X-Ray and Gamma-ray Astronomy

X-ray and gamma-ray detection is crucial to our understanding of AGN and BH-XRBs. However, their detection give rise to a number of challenges. Figure 3.1 depicts the problem in X-ray and gamma-ray astronomy. Particles of such high energies do not reach the Earth's surface, which makes detecting them directly on the ground impossible. As a result it is a requirement to attempt detection above the Earth's atmosphere, failing that, indirect methods are used and these methods are described in the subsequent sections.

3.1 X-Ray Astronomy

As can be seen in Figure 3.1, it is impossible to detect X-rays at low altitudes as X-ray photons are absorbed by particles in the Earth's atmosphere through, mostly, Compton scattering. X-rays are only detectable at high altitudes or from telescopes on board satellites. A few X-ray experiments are the Burst Alert Telescope (BAT) aboard the *Swift* observatory, the All-Sky Monitor aboard the *Rossi X-ray Timing Explorer* and the *Monitor of All-sky X-ray Image (MAXI)* aboard the Internation Space Station.

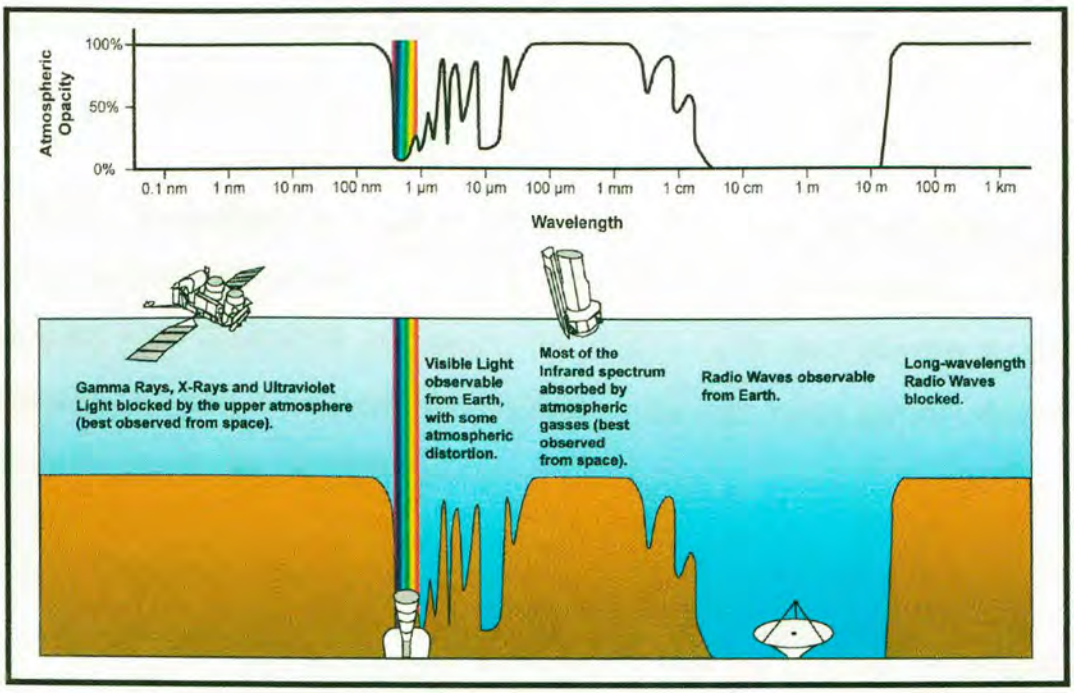

Figure 3.1: Atmospheric Opacity as a function of wavelength. Gamma-ray, X-ray and ultraviolet photons are blocked by the atmosphere and do not reach the ground. Non-harmful visible light is not absored and reaches the ground above sea level. However, in the Atmospheric opacity plot at the top it can be seen that the atmosphere is not completely transparent for visible light. Infrared waves are also absorbed by the atmosphere. Radio waves are visible from the Earth as the atmosphere is completely transparent to it, i.e. it absorbs no short wavelength radio waves. The far right of the figure illustrates how long wavelength radio waves are also completely absorbed in the upper atmosphere. Figure from [39]

3.2 Gamma-Ray Astronomy

Figure 3.1 also shows that the atmosphere is absolutely opaque to gamma-rays and thus these cannot be detected from the ground as in the case of X-rays. So ideally the best way to detect gamma-rays is from above the atmosphere [11].

One satellite-born experiment is the *INTErnational Gamma-Ray Astrophysics Laboratory* (*INTEGRAL*) launched by the European Space Agency in 2002 and covers an energy range of 15 keV to 10 MeV [40]. The *Fermi Gamma-ray Space Telescope* (*FGST*) launched in 2008 is another of its kind, which covers a different energy range. The main instrument aboard FGST is the Large Area Telescope (*Fermi*-LAT) which detects photons of energies ranging $20\text{MeV} \sim 300\text{GeV}$ [41]. The

BAT aboard *Swift* also detects photons with energies between 15 and 150 keV in the gamma-ray regime [42].

Although gamma-rays do not reach the ground, there is an indirect method of detecting them, through their interaction with particles in the atmosphere. When particles enter the Earth's atmosphere, they interact with other particles in the atmosphere, which is the mechanism explaining why high energy particles do not reach the ground (see Subsection 3.2.1).

3.2.1 Cherenkov Light

Cherenkov Light (CL) is the name given to the radiation produced by charged particles that move faster than light in an arbitrary medium. If the said charged particle moves faster than the speed of light in the medium, then the emitted radiation interferes constructively creating a faint blue light called Cherenkov Light. In fact the particle emits light over a range of the EM spectrum and its intensity peaks between 300 to 350 nm as can be seen in Figure 3.2. Therefore the light observed would be of a blue color.

The incident particle interacts with particles in the atmosphere by inverse Compton scattering or electron pair production near a nucleus. Subsequently, the energized electrons interact with other nuclei through Bremmstralung or scatter off other electrons creating an extensive shower of particles as the above processes are repeated a number of times. The electrons in these processes inherit substantial energies from the incident particle and thus move at relativistic velocities creating the CL. This CL is then detected by different instruments, but most commonly Imaging Atmospheric Cherenkov Telescopes (IACTs), discussed in Section 3.3.

Another method of detecting gamma-rays from the cosmos that produce extensive air

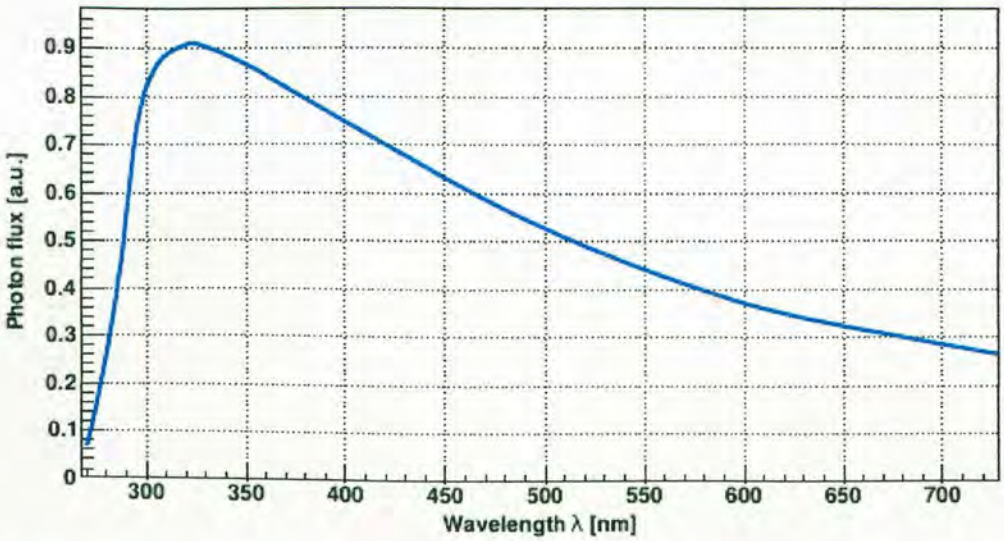

Figure 3.2: Photon flux of Cherenkov radiation over a range of wavelengths, with peak at 330 nm. Figure from [8].

showers (EAS) are "Air Shower Arrays". These arrays directly detect the paricles form the EAS. This means they must be at very high altitudes and can only detect gamma-rays that produce very large EASs, which means the gamma-ray must be of very high energies. The detectors of these arrays are many tanks of water spread out over a large area [43]. An advantage such detectors have over IACTs is that they can operate at any time and do not depend on the production of CL in the atmosphere. The CL they detect is rather produced in the water tanks.

3.3 Cherenkov Telescopes

In this section is an outline of the working principle of Imaging Atmospheric Cherenkov Telescopes (IACTs) for the detection of EM radiation described in Subsection 3.2.1. Cherenkov Telescopes (CTs) are optical telescopes that have the purpose of detecting the faint light, which has its origins from tremendously energetic cosmic particles.

Figure 3.4 depicts the working principles of CTs. Once the primary particle induces the air shower, many secondary particles have enough energy to emit CL at

Figure 3.3: Air shower array in Yangbajing Tibet, composed of 1848 detector elements [43]. Figure from [44].

an angle θ_C with the primary shower axis. It is an advantage to have a large surface area so as to collect as many photons as possible. Mirrors reflect the CL onto Photo-Multiplier Tubes (PMTs) which are fitted with Winston cones[1] to gather the light that would otherwise fall between PMTs. Furthermore, the cones reduce background light which would increase uncertainties in measurements [45]. As mentioned in Subsection 3.2.1, CL is not only produced by gamma-ray induced showers but also by any immensely energetic charged particle. Thus it is of interest to gamma-ray astronomers to distinguish between the different showers produced by different particles. There are a number different ways to do this and a few are outlined and discussed in Section 4.2.

Table: 3.1 describes the CTs that are or have been in operation in the world, H.E.S.S. in Namibia, VERITAS & Whipple in USA, FACT & MAGIC in Spain and CANGAROO in Australia (which has been decommissioned).

[1]Winston cones are light collectors with reflective inner surface that have a large aperture for collection and concentrates the collected light through a smaller aperture at its exit.

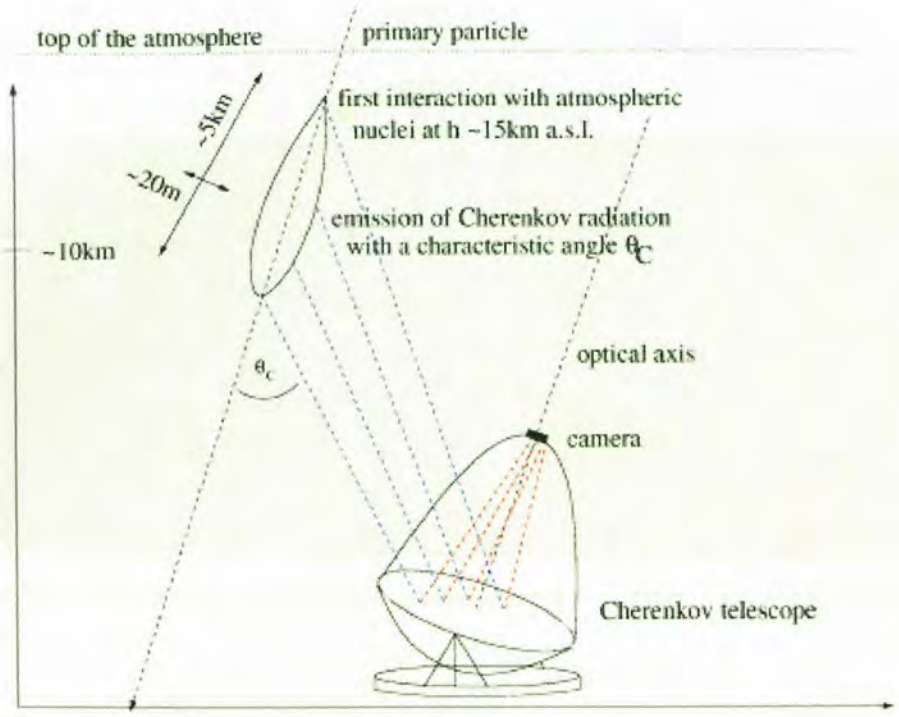

Figure 3.4: Schematic of CL detection by IACT's. The primary particle induces a shower of energetic particles which produce CL emitted at an angle of θ_C with respect to shower axis. Mirrors reflect light to a camera concentrated onto PMTs by Winston cones [9]

Table 3.1: Description of CTs that are or have been in operation with a few key characteristics listed. The field of view is the radial angle on the sky that each respective telescope can view at an instance [1,45,46].

Instrument	Altitude [m]	Tels.	Tel. area [m^2]	Total area [m^2]	Pixels	FoV [°]
H.E.S.S.	1800	4	107	428	960	5
	1800	1	614	614	2048	3.2
VERITAS	1275	4	106	424	499	3.5
FACT	2225	1	9.5	9.5	1440	5
MAGIC	2225	2	236	472	574	3.5
CANGAROO-III	165	3	57.3	172	552	4
Whipple	2300	1	75	75	379	2.3

3.3.1 H.E.S.S.

The High Energy Stereoscopic System is the primary instrument of this thesis. This is a system of IACTs, 4 arranged on the vertices of a square and the last in the center of the said square. H.E.S.S.-I (phase I) refers to the smaller telescopes (called CT 1 – 4),

Figure 3.5: High energy stereoscopic system located $\sim$ 100km south west of Windhoek, Namibia.

with 382 round mirrors each of 60 cm in diameter and an effective mirror surface area of 107 m^2, each [45]. The cameras of CT 1 – 4 consist of hexagonal arrays of PMTs each analogous to a 0.16° diameter patch on the sky. H.E.S.S.-II (phase II) refers to the addition of a fifth telescope (called CT 5) in the center of the original array added in October of 2012. This detector consist of 876 hexagonal mirrors as the building blocks of a 614 m^2 reflective surface area. Its finely pixelated camera allows for state of the art resolution as far as CTs are concerned.

3.4 *Fermi*-LAT

The *Fermi*-LAT (hereafter referred to as LAT) is the leading space based gamma-ray detector. A schematic of its working principles can be seen in Figure 3.6. A gamma-ray is detected when it passes the anti-coincidence scintillator, which has the purpose of detecting charged particles, i.e. it rejects background. Its source is reconstructed from the path traversed through multiple silicon strips by the electron-positron pair. When the photon passes through the silicon strips, it passes near a silicon nucleus and is thus converted into matter by the pair production of the electron and positron. The energy of the gamma-ray is reconstructed by measuring

the energy deposited in the calorimeter [41].

As is well known, CRs are much more dominant in the Cosmos compared to

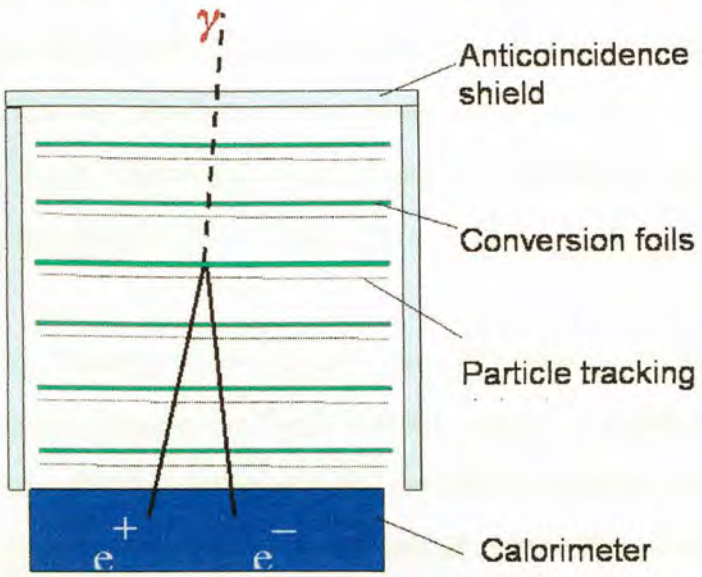

Figure 3.6: Schematic depicting the working principles of *Fermi*-LAT. A gamma-ray passes freely through the anti-coincidence plastic scintillator tiles while CR interact with it and are subsequently rejected as background. The gamma-ray undergoes pair production near the nuclei of the conversion foil. The particle (gamma-ray) is tracked by silicon strips and its energy predicted by the cesium iodide calorimeter at the bottom [41, 47]. Figure adapted from [48].

gamma-rays, dominating by 3 to 5 orders of magnitude [47]. The anti-coincidence detector surrounds the tracker and provides rejection of charged particles.

3.5 Ryle Telescope and AMI Large Array

The Ryle Telescope was a linear array of 12.8 m Cassegrain antennas which was replaced by the Arkminute Mikrokelvin Imager (AMI) large array, the re-built and reconfigured Ryle Telescope. The AMI consists of eight 12.8 m dishes and observe a range of frequencies (13.9 – 18.2 GHz) [49, 50]. The AMI is located at the Mullard Radio Astronomy Observatory near Cambridge and is operated by the Cavendish Astrophysics group. This array has a primary purpose of studying galaxy clusters through Sunyaev–Zel'dovich imaging [51].

3.6 X-ray Telescopes

The All-Sky Monitor (ASM) aboard the *Rossi X-ray Timing Explorer* monitors the sky in the energy range $1.5 - 12$ keV. The instrument consists of 3 scanning shadow cameras mounted on a motorized rotation drive to view different regions. Each of these cameras contain position-sensitive proportional counters viewing the sky through a slit mask, measuring strengths and displacement patterns of shadow patterns cast by the observed X-ray sources [52].

The Burst Alert Telescope (BAT) aboard the *Swift* observatory has the primary purpose of detecting Gamma Ray Burst (GRBs), which are flashes of gamma-rays originating from collapsing stellar masses into BHs or compact star mergers into BHs [5]. This is made possible by its large field of view (FOV, 1.4 sr) cameras [42]. The BAT telescope observes in energies ranging from 15-150 keV. Its working principle is not so much different form a Geiger counter. While searching for GRBs, the BAT simultaneously accumulates an X-ray survey of the entire sky [42].

The *Monitor of All-sky X-ray Image* (*MAXI*) is part of the Japanese experimental module aboard the Internation Space Station (ISS). MAXI maps the X-ray sky with energies ranging from 2-30 keV making it a little more sensitive to lower energies than BAT, albeit still second the ASM [53]. MAXI not only monitors the sky for GRBs but also takes long term data of X-ray sources, which makes their data desirable to study variability on long time scales [53]. Although MAXI has a wide FOV, observations are sometimes disrupted by the orbit of the ISS. The structure of ISS obscures the FOV of the MAXI cameras and is therefore another reason that could disturb long term observations of specific sources. MAXi can also not be used for pointing because the ISS rotates such that one side of it always faces the center of the Earth and the other to the sky, and since MAXI is simply a payload it can be used for observations but not for pointing [53].

Chapter 4

Data Analysis

In this chapter is an outline of all the data sets used in this thesis and the techniques employed to analyze them. The H.E.S.S. data, important for the focus of this work, is firstly introduced followed by the light curve data from the different radio, X-ray and gamma-ray telescopes.

4.1 DATA

4.1.1 H.E.S.S. Data

As part of the H.E.S.S. collaboration, the University of Namibia has full access to all data sets taken by the H.E.S.S. telescopes since their inception in 2002. The data sets are in the Storage and Analysis Software for H.E.S.S. (SASH) format and are accessed as ROOT[1] files. This format allows one to efficiently navigate and perform operations on the said data set without worrying about memory limitations. The SASH format allows the H.E.S.S. collaboration to store data from the numerous subsystems that make up the instruments, in one file.

These files were then accessed using the ROOT framework and C++ programming. Different data classes are stored in one data set in the form of trees, e.g. the run quality tree which stores information such as the sky radiometric temperature as taken from each telescope, this information is useful in understanding the "quality" of the

[1]ROOT is data analysis framework developed by European Organization for Nuclear Research also known as CERN, initially for data analysis of data from the large hadron collider.

observations..

As analysis sensitivities are often given in terms of percentage flux from the Crab Nebula, much data from the Crab Nebula already exists in every configuration the stereoscopic system has ever been in (e.g. old and new cameras etc.). As this is a well studied source in the field of high energy astrophysics, data from this source taken in 2015 with CT2–5 was used and photons from a source of its kind were also simulated for this thesis.

4.1.2 Light Curve Data

Light curve data from the direction of Cyg X-1 and Cyg X-3 used by Zdziarski *et al.* in [33] and [49] was used. This encompasses radio light curves between MJD 50226 – 53902 from the Ryle telescope and between MJD 54573 – 57748 from the AMI large array at 15 GHz, as published in [38], *Fermi*-LAT light curves and X-ray light curves from the ASM and BAT. The ASM data is in 3 bands, 1.5 – 3 keV, 3 – 5 keV, 5 – 12 keV, spanning 5783 days from MJD 50087 – 55870 while that from the BAT spans 4461 days from MJD 53416 – 57848 in one energy band 15 – 40 keV. Light curve data from MAXI was also used and spans only 2819 days between MJD 55058 – 57877 in 3 energy bands: 2 – 4, 4 – 10 and 10 – 20 keV.

All the above mentioned data was a result of taking an average of the light curve fluxes in 1 day bins. The original un-binned LC data was also available if the need arose to seek finer features in cross-correlations.

4.2 Analysis Methods

The first step in analyzing the H.E.S.S. data was to perform "shape cuts" on the images taken. These shape cuts were done by rejecting images with an amplitude less than 60 photo-electrons per telescope, rejecting images where the center of the shower image was more than 2° away from the center of the camera and, for stereo

event reconstruction, at least two telescope images must meet the shape cuts criteria. A model was then fitted to the shower image to reconstruct the inducing showers parameters. The model was generated using Monte Carlo simulations of the Cherenkov Light distribution of charged particles in the EM showers, taking into consideration light collection efficiency of the detectors, atmospheric absorption, shower morphology, etc. This distribution was determined by longitudinal, lateral and angular distribution of charged particles in the shower with respect to the shower axis. The contributions of night sky background (NSB) was also modeled based on a statistical analysis. The actual shower images were then compared, pixel by pixel, to images produced by the simulated showers and the parameters of the best fit images were then assumed as the parameters of the actual shower inducing particle. A goodness of fit approach was taken to do the comparison between the model and data [54]. It is worth noting that there are different types of analyses that could be done with this same data. However it seems, at least for now, that between the two methods mainly used (Hillas Parameterization and Model++), the model approach grants a better background rejection [54]. The results in [54] were achieved by only using one separation variable versus the entire Hillas analysis. Thus Hillas type analysis was not considered in this work [55].

4.2.1 Paris Analysis Software

The Paris Analysis software was developed to analyze H.E.S.S. data using either the model/template fitting or the older Hillas Parameters. The analysis part of the software was written in C++ and wrapped with a python graphical user interface. In the context of this thesis, this software was installed on the high performance computer (HPC) at the University of Namibia (UNAM) and used to analyze the data. There were a number of steps involved in the installation process. Firstly, the dependencies needed to be installed owing to the fact that the software as a whole is a combination of many different codes which use many different interpreters or compilers. Since this requires a number of changes, it was decided to create an

environment in which the software would run after its installation so as to allow other groups a standard system to work on in the future. The main dependencies are ROOT and python. A list of other dependencies can be found in appendix A. The ROOT version installed is version 5.34.36, the reason being that ROOT is always in development and commands are often changed. Therefore since the Paris Analysis software was written while using version 5.34.36 as the active version, it was imperative to use this version for our installation to avoid unimportant errors. After downloading ROOT, it was configured using a gcc compiler compatible with this version of ROOT and the HPC server architecture, with the packaged "configuration" file. In the configure command, enabling another set of packages not normally installed as standard was important as they are needed to run all the Paris analysis software. This process revealed the additional "non-ROOT" packages that needed to be installed before using the "make" file to build ROOT. An example of a dependency required is *cfitsio* which is a library for fortran and C providing simple high-level routines for reading and writing image files in the Flexible Image Transport System (FITS) format. Appendix B has a list of all dependencies and commands for discovering dependencies that still require installation. Once all the dependencies were installed, the make command was used to build ROOT. A procedure of the same nature was repeated for the installation of *AstroRoot* which is simply an extension of ROOT for astronomical data analysis.

For the graphical user interface (GUI), the HPC required *gtkextra* which is generally a library of widgets for creating GUIs. This is not readily available for all operating systems and thus collaborators have had the idea to have one rpm package readily available for the collaboration. An rpm package is a executable file designed for Red Hat Enterprise Linux (RHEL) operating systems. Once *gtkextra* was installed, the Paris analysis software was then downloaded from a server at Humboldt University in Berlin, including *scons* for dynamic compilation of source code and environment. This is similar to the "make" building process. *Scons* is more reliable in that it is a cross platform and cross-language faster way of building software compared to

"make".

All the above steps were done on the server, to make it possible to analyze data on it. To be able to analyze data on the computing nodes, the dependencies had to be installed on them as well. An intuitive way of doing this was to install dependencies on one image file and boot all the nodes with this image file. Once the installation on the image was done, the nodes were rebooted and the software was ready to use. The computing nodes also required internet access to analyze the H.E.S.S. data using the Paris analysis software, so permissions were given to allow them to communicate with only one IP address in Lyon. This connection was required for collaboration membership verification.

The Paris Analysis' graphical user interface eases use of the analysis software. Figure 4.1 is a screen shot of the Paris analysis software, as installed on the HPC at UNAM. The entire installation was tested by analyzing a few runs on 3 different clusters with the same software installed. This was done to ensure dependable results that can be reproduced. The cross-validating clusters were in Lyon at and Johannesburg. These clusters are maintained by experienced groups in the collaboration. The data to be analyzed was selected from the 2015 and early 2016 runs of the Crab nebula. The run list consists of 7 runs taken with a telescope configuration involving CT2–5. These runs were selected based on weather conditions at observation time, calibration status, number of available telescopes and immediate availability of data. The details are outlined in Section 5.1.

4.2.2 H.E.S.S. Data Analysis

A standard analysis was conducted by choosing a profile or creating one. Here a profile entails the analysis criteria used, such as separation method and shape cuts. In the context of this work, it was required to have information of different reconstruction methods, i.e. mono reconstruction, stereo reconstruction with CT1–4 and stereo reconstruction with CT1–5 as one array. For this reason, a combined

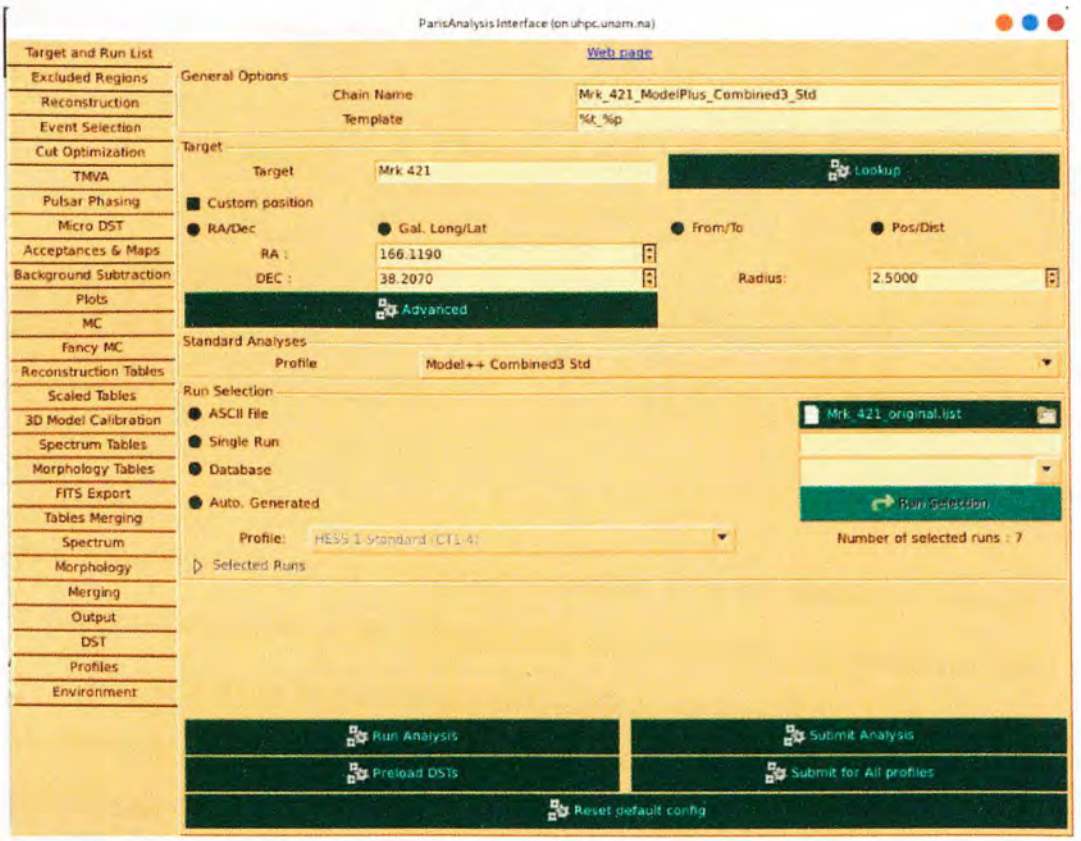

Figure 4.1: A screen shot of the Paris Analysis Software as installed on the HPC at the University of Namibia.

analysis profile, which attempts reconstruction of all 3 types and chooses the one which gives the best detection significance while maintaining a reasonable error, was used. The selection cuts used for each profile can be seen in Table 4.1, whereas the mean scaled shower goodness (MSSG), primary depth and θ^2 are described in Chapter 5. There are variations to these standard shape and selection cuts that could be used. Some variations come readily available with the software. The GUI allows for change of these variables in any form. However some "unorthodox" cut combination may have no simulations available and therefore attempting an analysis under such conditions fails.

The GUI essentially generates a bash script which is submitted to the computing nodes. If it was required to fine tune the analysis with options not available in the GUI, it would be done in the bash script. In this work all option changes were performed with the GUI and there was no cause of adjusting the generated bash script.

Table 4.1: Table of image shape cuts and event selection cuts done in different analysis profiles.

	Shape Cuts			Selection Cuts		
Profile	minimum image amplitude [p.e.]	nominal distance [deg]	minimum CTs	MSSG	Primary Depth	θ^2 [deg^2]
H.E.S.S. I	60	2	2	[-4, 0.3]	[-1.1, 4.4]	0.010
H.E.S.S. II	60	2	2	[-4, 0.9]	[-1.1, 3.4]	0.006
CT 5 Mono	60	1.4	1	[-4, 0.7]	[-1.1, 1.3]	0.015

To study the distributions of separating variables, it is of interest to produce Micro-datasets (Micro-DSTs) which would store values for separating variables given to each event. To produce Micro-DSTs, each is event is reconstructed according to the profile selected and its reconstruction parameters are stored in the Micro-DST. Micro-DSTs are produced on a run by run basis, i.e. each Micro-DST has only the reconstruction information of events in that run. To analyze the Micro-DSTs all at once, a *TChain* object had to be created. A *TChain* is a collection of files containing *TTree* objects. The *TTree* is the name given to an object with a list of independent branches which all contain different buffers (stored data or leaves). If the *TTrees* have the same name then all branches, and consequently leaves, are placed under one tree and one may manipulate the leaves as a whole data set. The code written for this thesis to produce this *TChain* from the "raw" Micro-DSTs is shown in appendix B.

The shower simulations produce data sets that are in the same format as that of the actual data and thus are handled the same. Showers induced by hadrons and high energy photons are simulated and compared to actual data, to produce an adjustment to the already existing cuts mentioned in Table 4.1.

4.2.3 Light curve cross-correlations

A light curve is a plot showing the brightness of an object over a period of time. This brightness is given in terms of the photon flux.

To test for lags, the method proposed by Zdziarski et al. in [49] was used. This

method involves searching for pairs of data points in two discretely defined light curves that have a lag of a certain range and use them in the calculation of Pearson's Correlation Coefficient according to Equation 3 in [49]. There are a number of pre-written programs that can do this job, such as z-transformed discrete correlation function (ZDCF) [56] and pyDCF written in python [57], etc. However, in this work, the option to write a new program in python and cross reference with older ones was used. Additionally, these pre-programs had limits unknown from the start. Firstly, the newly written program was used to confirm the results produced in [49]. The same data used in [49] was used to reproduce the cross- and auto-correlations for gamma-rays with 15 GHz radio emission and for X-rays of different bands with 15 GHz radio emissions.

The method, was to calculate the Pearsons correlation coefficient $2N$ times for two discretely defined light curves x_i and y_j, where N is the total shift in time, $i = 1, ..., I$ and $j = 1, ..., J$. The Pearson's correlation coefficient is then defined as,

$$r(\Delta t) = \frac{\sum_{i=1}^{K}[x_i - \bar{x}][y_i - \bar{y}]/K}{\sigma_x \sigma_y} \tag{4.1}$$

where x_i and y_i are chosen for light curve points that pass the criteria,

$$\Delta t - \delta/2 \leq t(y_i) - t(x_i) < \Delta t + \delta/2, \tag{4.2}$$

δ is the bin size, σ the standard deviation and K is total number of x_i, y_i pairs. Thus any code using this method essentially needs to choose light curve points that are $\delta/2$ distances apart, create two new data sets, one with a light curve of x_i passing the criteria in Equation 4.2 and the other of y_i. The code then calculates $r(\Delta t)$.

First a linear repetitive approach was taken to calculate these cross-correlations, i.e. correlating light curves by means of a functions $2N$ times for every value of Δt. This was an in-efficient way to do it. Large data sets, which was the case for the un-binned LCs, took a very long time to correlate, the longest of which was ~ 66 h.

Another method attempted was to calculate, in vector form, the difference between all possible pairs and place the result in a $J \times I$ matrix, and then use a mask to query values in the matrix, and thus pairs, that pass the criteria in Equation 4.2. This method performs splendidly, decreasing computational time by a factor of 27. However, it suffered the fatal flaw that the large $J \times I$ matrix was to be stored in memory. Since the values in the matrix are floating point numbers, the memory required would be $(J \times I) \cdot 64$ bytes. Thus, a system running on 16 Gb of RAM is limited to a matrix of $2.5 \cdot 10^8$ numbers. This seems large, however in the context of datasets composed of multiple (~ 10) readings per day, over a long period, this is at least an order of magnitude too small.

The method that works best with shortest computing time required reformatting of Equation 4.1 and rewriting standard deviation as the difference between the sum of the squares of the values passing the criteria in Equation 4.2 and square of the sum. The numerator of Equation 4.1 can be re-written as $< xy > - < x >< y >$. The new equation now allows for 3 nested *for* loops to complete the entire cross-correlations. The first does a check for criteria 4.1 and immediately computes the sums of x and y and their squares. The second computes the differences as required in the equation and the third computes the standard deviation according to a similarly reformatted Equation 5 from [58].

All the above mentioned techniques provide accurate results. The only, and perhaps most important, difference is their computational performance. The third method was the most time efficient and computationally conservative method.

To further study the cross-correlations in detail, it is important to split the light curves into the different states of Cyg X-3. For simplicity, the data was split, where needed, into hard/intermediate and soft states, i.e. the dates where Cyg X-1 was in the hard/intermediate and soft state. This state is determined by the spectrum observed in

Table 4.2: Outline for time intervals when the Cyg X-1 was in hard/intermediate state.

start [MJD]	end [MJD]
50085	50222
50308	51845
51858	52167
52205	52237
52545	52801
52853	53003
53025	53265
53292	53368
53385	55387
55674	55790
55895	55940
56035	56087
56722	56748
56760	56845
57012	57045
57105	57265
57331	57880

that time by the source. Since the radio/X-ray correlation has similar properties in both hard and intermediate states [33], they are treated jointly. Table 4.2 illustrates the lengths for hard/intermediate state duration in MJD. For all other days, the source was considered to be in a soft state.

Chapter 5

Results

This chapter outlines the results obtained by the methods discussed in Chapter 4. Firstly, confirmation of the accuracy of the cluster is presented followed by the detailed primary depth studies for simulated and experimental data from the Crab nebula. Lastly, cross-correlation results are presented after initial method validation.

5.1 Cluster Testing

The installation of the software on the UNAM cluster was successful and cross-validation results suggest the software performs identically to the software installed on the clusters in Lyon and Johannesburg. This was not surprising as assurances were made that the same version of the software was used on all clusters. Additionally, this gives a level of confidence one may have concerning results produced on the local cluster.

Figure 5.1a shows the results for excess gamma rays detected in the 2.9 hours of observation in Right Ascension (RA) and Declination J2000 coordinates. A total of 1546 events have been classified as having come from the source. There is a clear access of events coming from a point source and hence the significance map in Figure 5.1b boasts a 73σ detection significance. Although it has only been observed for 2.9 hours, it was understandable to have such a high significance as the Crab Nebula is very bright in gamma-rays and is well known as the "standard candle" in

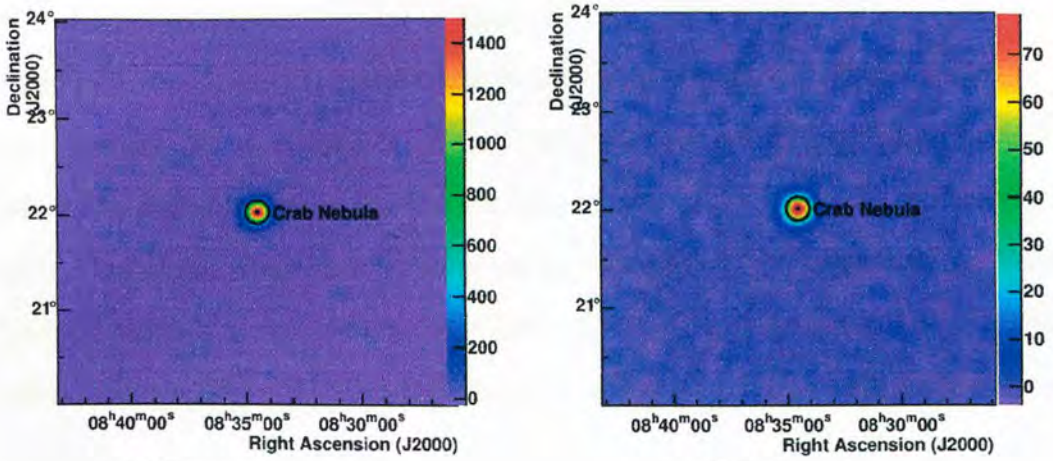

(a) Gamma-ray excess sky map.

(b) Significance sky map.

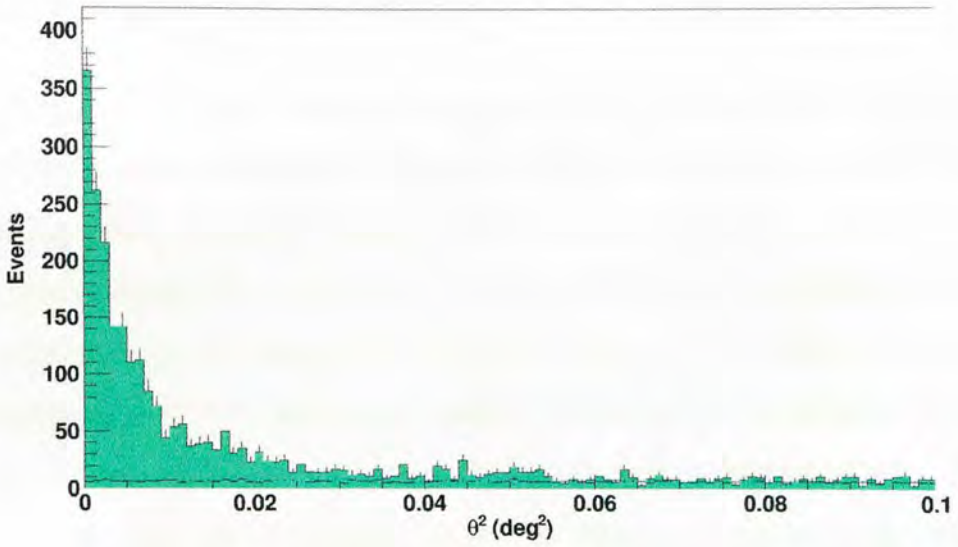

(c) Theta squared distribution showing the squared reconstructed off set.

Figure 5.1: Results for 2015 Crab Nebula data. a) and b) Shows a map of right ascension and declination of the gamma-ray sky at the position of the Crab nebula. The color scale in a) shows the number of excess events at the respective positions and in b) the gamma-ray detection significance. In c) can be seen the square of the angle between the reconstructed position and the actual source position.

very high energy gamma-ray astronomy. Figure 5.1c shows the square of the angular distance of reconstructed directions of excess gamma rays from the source, where zero squared degrees is the center of the source. This plot shows all reconstructed directions from the source for all access events which number 1677 and from the Table 4.1, since the data was taken with a combination of CT1–4 and CT5 one can see a cut of 0.006 will be applied and thus leading to an excess sky map of only 1546 events.

The energy spectrum can be seen in Figure 5.2. An exponential cut off power law was fitted to this spectrum. The power law fit gives an index of $\Gamma = 2.262 \pm 0.055$ and a cut off energy $E_c = 9.263 \pm 1.913$ TeV. These results are is in agreement with the results published in [45], where a spectral index of ~ 2.3 was calculated. The result presented in this work is more accurate as the method used then was the Hillas method and it is clear now that the Model analysis is more accurate than the older Hillas method [54]. This curve fits the data with a $\chi^2 = 24.3$ with 34 degrees of freedom.

5.2 Primary Depth distribution studies

The depth of first interaction or primary depth (PD) is reconstructed using simulated templates similar to all other separation variables. This variable is second to the mean scaled shower goodness (MSSG) selection cut and is always given in terms of radiation lengths $X_0 = 36.62\ \mathrm{g\,cm^2}$ for air. For the 2015 Crab Nebula data set, all events passing the shape cuts are reconstructed to give a value for all shower parameters. All this data can be found in the Micro-DSTs described in Subsection 4.2.2. There are a number of parameters for all events in the Micro-DSTs. A few of these are: the time of the event, number of telescopes triggered by the event, etc. More importantly, since a combined analysis was performed, the selection parameters are given in terms of the different analysis profiles and the one chosen by the algorithm as having the best result. Therefore, for every analysis, HESS I, HESS II and CT5-Mono, there are leaves containing MSSG, PD, θ^2 reconstructed energy, etc. The distribution of PD, i.e. a histogram describing the frequency (number of events) of all events in the data set can be seen in Figure 5.3. This histogram shows a total of 867,276 events. The histogram exhibits an extreme cut off at $PD = 9, -2\ X_0$ after peaking at these values. Other peaks are a seen at $PD = 5\ X_0$ and$PD = 1\ X_0$, which is the absolute maximum of the histogram. All these events have passed the initial shape cuts. This was however the distribution that has been computed as the "best" for the combined analysis, i.e. of all single reconstruction method this was

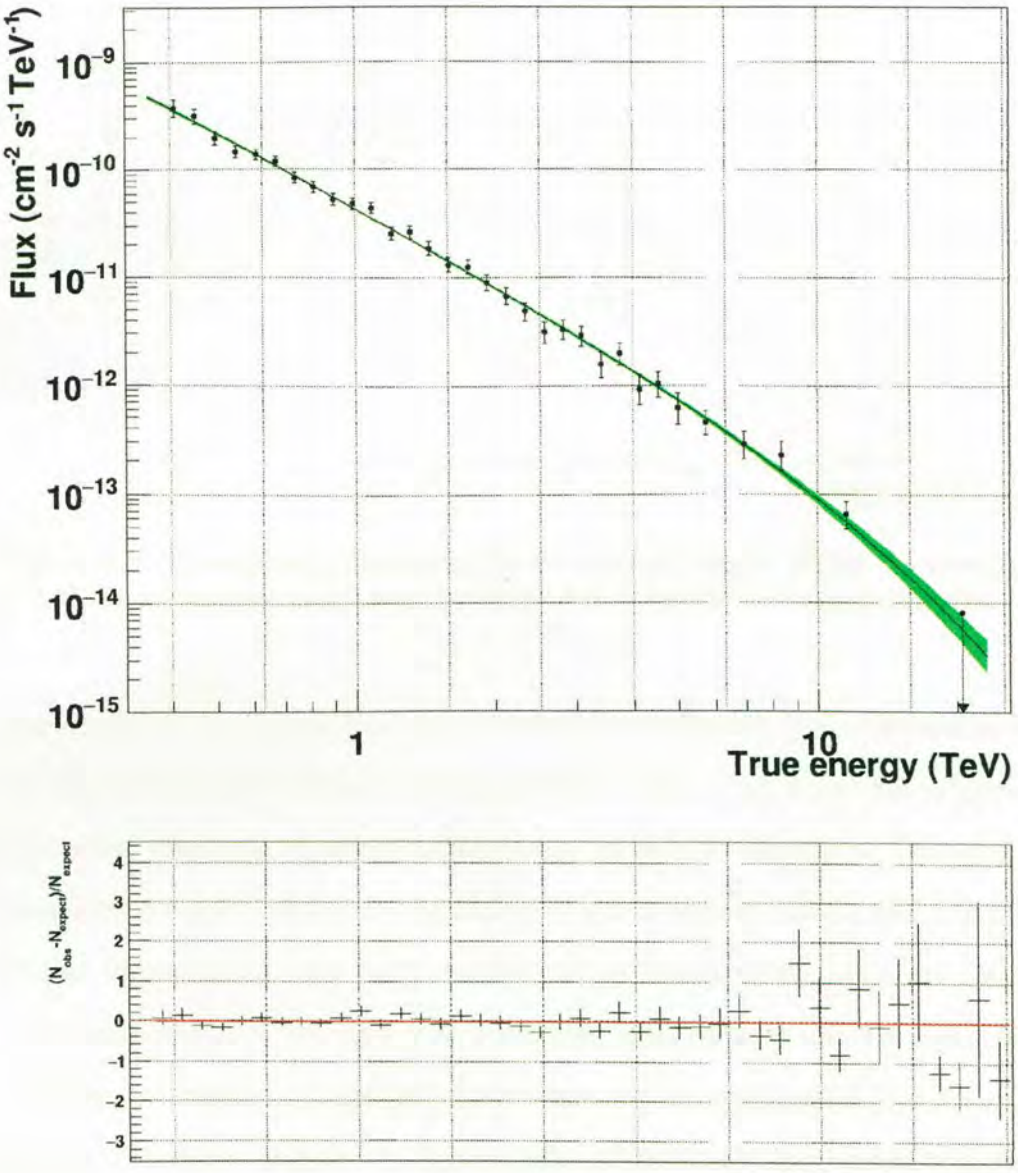

Figure 5.2: Above, the energy spectrum with a power law of index $\Gamma = 2.262 \pm 0.055$ and an exponential cut off energy of $E_c = 9.263 \pm 1.913$ TeV can be seen fitted to the data. The green shade is the 1 σ statistical error. Below, the fit residuals can be seen for each energy.

found to be the best. As this combined analysis was the analysis under scrutiny it was of interest to have a closer look at the distributions of each reconstruction configuration. Figure 5.4 shows these distributions, where Figure 5.4a is for the stereo reconstruction of H.E.S.S. I, i.e CT 1–4, Figure 5.4b for H.E.S.S. II, i.e. CT 1–5

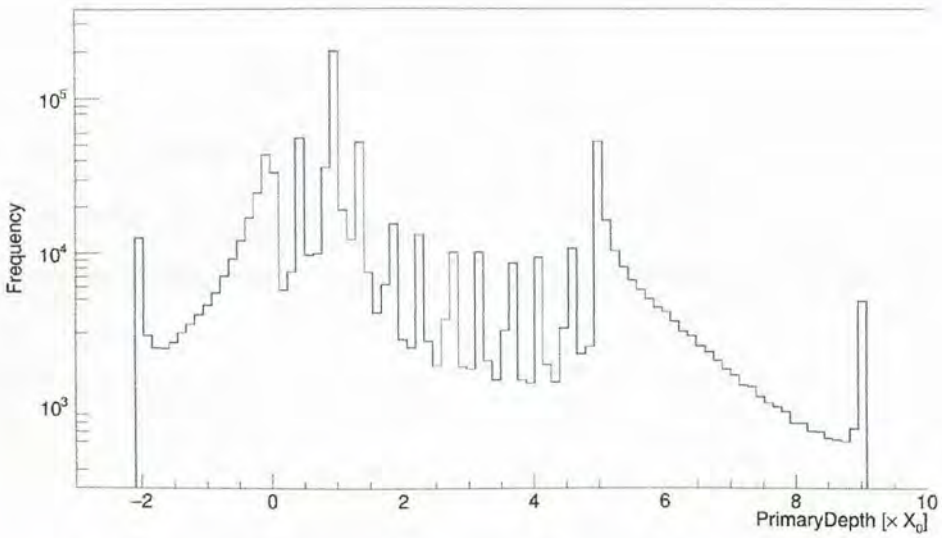

Figure 5.3: Primary depth distribution for the standard analysis (HESS II), showing the 867,276 events that have passed the initial shape cuts. Frequency is in logarithmic scale.

reconstruction, and Figure 5.4c for CT5 mono-reconstruction only. Characteristic to all these histograms in Figure 5.4 is a peak at $-1X_0$. This value was assigned to events that could not be reconstructed in that specific configuration. This could be caused by a number of factors. Immediately it can be seen that the H.E.S.S. I & II cannot reconstruct a very large number of the events in this data set yet CT5 mono-analysis does a better job at reconstructing most of the events. For this data set, there are two orders of magnitude more events not reconstructed in H.E.S.S. I & II than in CT5 mono-analysis. In Figures 5.4a and 5.4b there are 3 peaks observed at $PD = 9,\ 5,\ -2\ X_0$ which do not pass the selection cuts for the both these configurations (see Figures 5.5a and 5.5b).

To continue the analysis a filter had to be used to remove all these events that have an exact PD reconstructed value of $-1X_0$. Additionally to study the distribution of events that have been reconstructed by CT5 and have more than one telescope triggered another filter was required. For the Micro-DSTs, filters are simply applied by specifying a cut in the "active cut" section. Applying multiple filters, requires manually writing one line of code using the *Draw* function and C++ syntax.

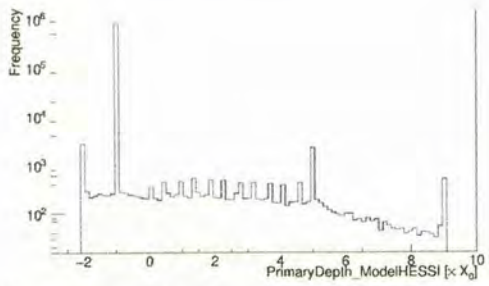

(a) Primary Depth histogram in log scale for H.E.S.S. I stereo reconstruction.

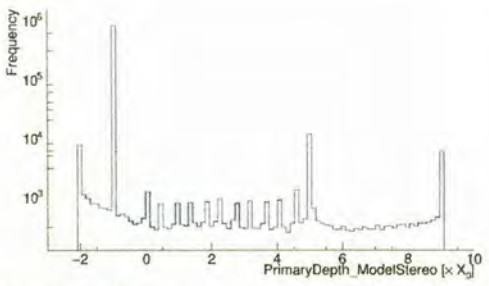

(b) Primary Depth histogram in log scale for H.E.S.S. II stereo reconstruction.

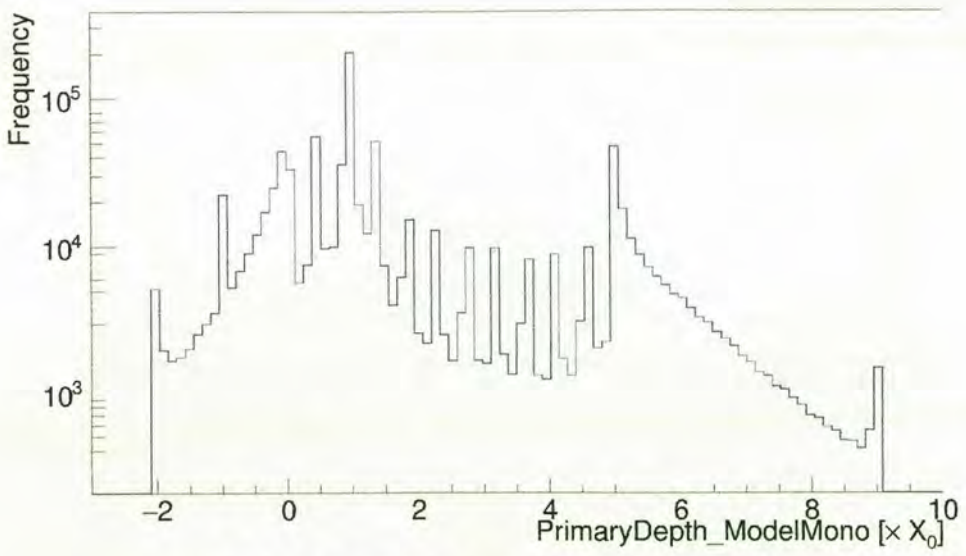

(c) Primary Depth histogram in log scale for CT5 Mono reconstruction.

Figure 5.4: Primary Depth distribution for different reconstruction configurations. In a) Primary Depth values for HESS I reconstructions are plotted in a histogram with a logarithmic scale. In b) primary depth values for HESS II reconstructions are plotted in a histogram with a logarithmic scale. This is for CT2–5. In c) primary depth values for CT5 mono-reconstructions are plotted in a histogram with a logarithmic scale. In all histograms a peak at -1 X_0 is observed. This corresponds to failures to reconstruct the event in that specific reconstruction profile. An example would be an event that triggered CT1–4 and not CT5 will fail to be reconstructed in CT5 mono-reconstruction configuration.

Figure 5.5 shows different PD reconstructions with different filters or cuts applied. A filter to remove events that have PD values of exactly $-1X_0$ has been applied to all further distributions. Figures 5.5a and 5.5b show in red lines where cuts are applied in the H.E.S.S. I and H.E.S.S. II configurations, respectively. The former distribution has only 22,058 events while the latter 61,942 events thus, out of all the events detected by the CTs, only 2.5% could be reconstructed with CT1–4 and 7.1% with

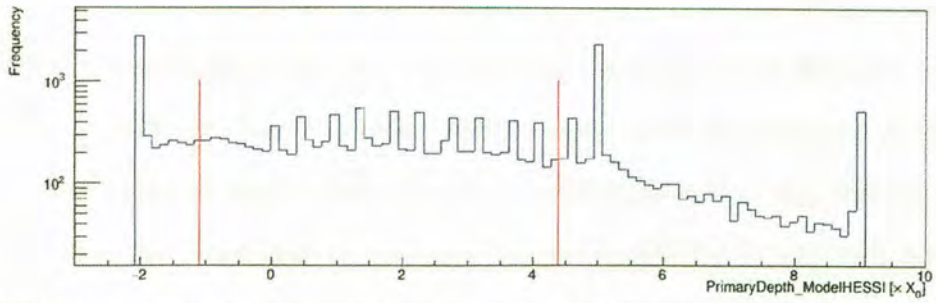

(a) H.E.S.S. I PD distribution for only events that could be reconstructed with CT 1–4 only and red lines depicting standard cuts to be applied to this variable.

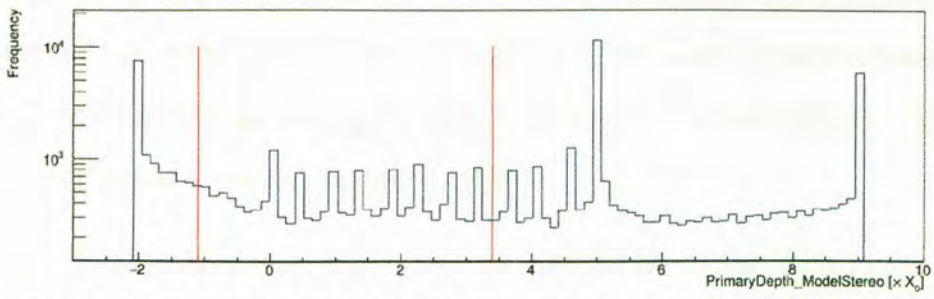

(b) H.E.S.S. II PD distribution for only events that could be reconstructed with the entire array, CT 1–5, showing the standard cut lines to be applied.

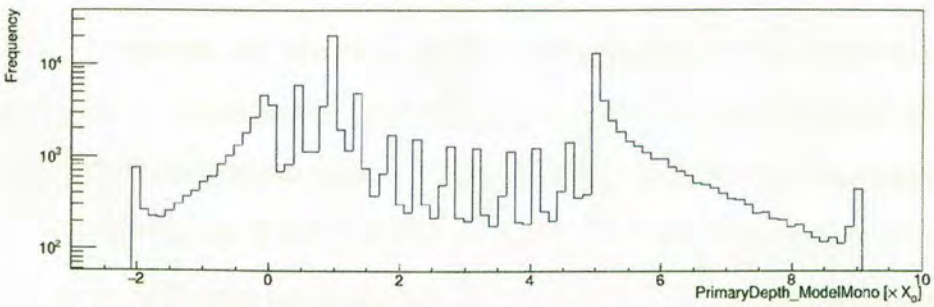

(c) Primary Depth distribution for CT5 mono-reconstructed events which triggered more than one telescope.

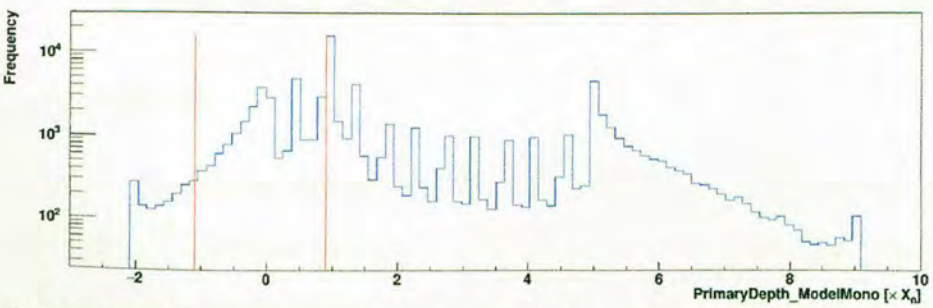

(d) PD distribution for CT5 mono-reconstructed events which triggered a minimum of 2 telescopes with mean scaled shower goodness cut applied and depicting where standard cuts would be applied to PD.

Figure 5.5

CT5 included. Figure 5.5c shows the distribution of the reconstruction of most interest in this work: mono-reconstructed events that have triggered more than one telescope. This distribution shows that over 112,492 events detected are, with absolute certainty, not muons as a muon could not trigger more than one telescope and the probability that two muons would hit two different telescopes at the same exact time (with an error of nano second magnitude) in such a way that the "event" would pass the shape cuts is very slim. This confidence is not well taken into consideration in the combined analysis. Such events account for 13% of the entire data set. When applying MSSG cuts, it can be seen that only 73,949 events survive. Figure 5.5d shows this distribution and in red lines the standard mono-reconstruction cuts. With the PD standard cuts applied, only 41,464 events survive. This is a significant amount, however, it can be improved upon.

5.2.1 Shower simulation studies

Shower simulations are crucial in gaining understanding of the behavior of these distributions. Consequently, gamma-rays and protons are simulated and their subsequent PD distribution studied. The parameters used for simulating gamma rays are 180° south (in the H.E.S.S. reference frame), 18° zenith angle and 1.5° off-axis angle[1] for the telescope configuration and a source of an energy spectrum obeying a power law of spectral index $\Gamma = 2.4, 2.6$, similar to that of the Crab Nebula [2, 45].

Photon Simulations

The photon simulations essentially grant us the ideal distribution for the PD reconstruction in different telescope configurations, i.e. this will allow us to understand what the distribution would look like if all events were triggered by gamma rays.

[1] i.e. the angle between the shower axis and the telescope axis.

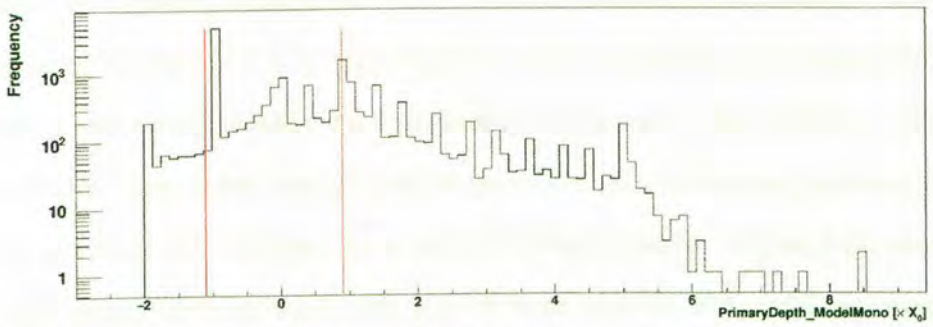

(a) PD distribution for events that could be reconstructed with CT5 alone, with no $PD = -1X_0$ filter applied. This histogram has 16,174 events that have been reconstructed and a logarithmic frequency scale. The reconstruction failed for 4,848 events which gives the rise to the peak at $-1X_0$. The red lines show where the PD cut will be applied.

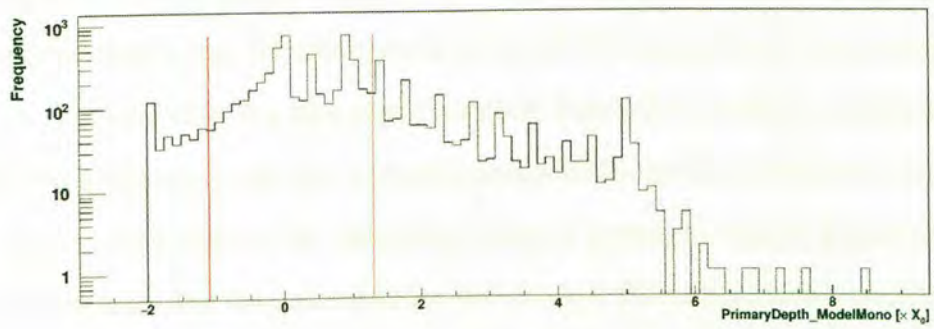

(b) PD distribution for mono-reconstructed events that have triggered more than one CT. Here a filter has now been applied to remove the 4,848 events that failed to be reconstructed and to remove events that only triggered one telescope. In this histogram is seen 7,045 events and in red the cuts to be applied to this variable.

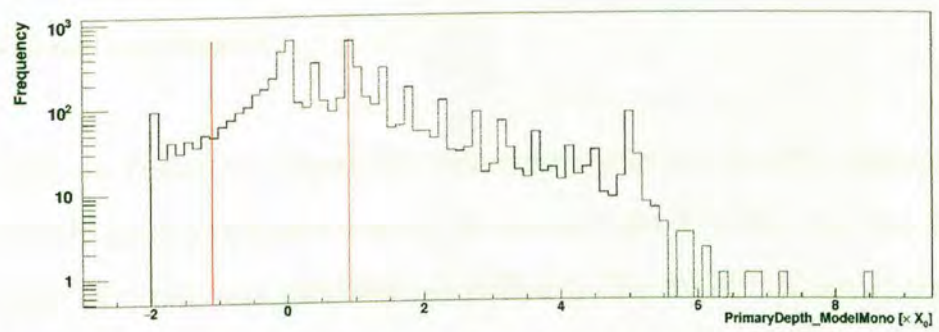

(c) PD distribution for mono-reconstructed events with one more filters applied, the MSSG cut. In this histogram is seen 5,923 events, meaning 1,122 events could not survive the MSSG cut. Standard cuts to the PD are shown in red.

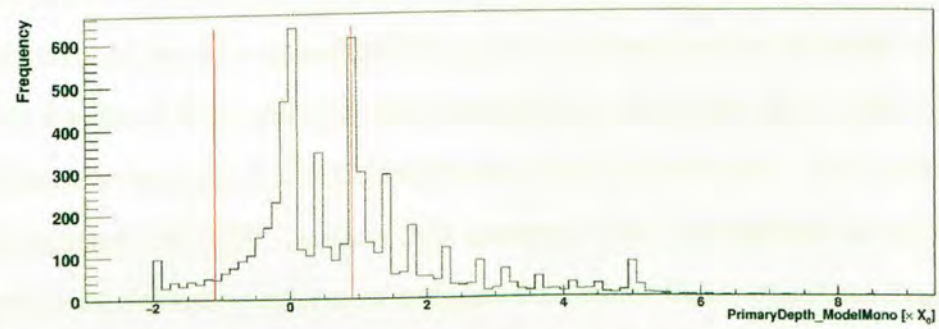

(d) PD distribution for mono-reconstructed events triggering two telescopes and passing MSSG cut criteria, with frequency not logarithmic. Standard cuts to the PD are shown in red.

Figure 5.6: Results for $\Gamma = 2.4$ spectral index photon source simulations. Here c) and c) are the contain the same data but different y-axis scales.

Figure 5.6 presents the results for $\Gamma = 2.4$ spectral index results. The events simulated here are 647,311. Although the events simulated are so many, only a few were reconstructed. Most events are lost by shape cuts as the off-axis angle used is significant. This is the best off-axis angle to use as it simulates gamma-rays whose shower axis is 0.5° off the center of CT5's field of view. Figure 5.6a shows only 16,174 events survived shape cuts and of those only 11,326 could be reconstructed with CT5 alone. Of these events 7,045 have triggered more than one telescope, this distribution can be seen in Figure 5.6b. This distribution bears some resemblance to the actual data at low PD values. As these are all PD values for photon reconstruction, a lower PD cut than that presented (in red) in Figure 5.6c could be considered. This plot has 5,923 events, as all events not passing MSSG cut have been removed. As this is quite a small number, the same distribution is presented without logarithmic scale in Figure 5.6d. For these simulations, the standard PD cuts include a majority of the events whose reconstruction could be improved by increasing the upper and the lower limit by $\simeq 1X_0$. To make sure this would work, the hadron simulations have to be taken into consideration.

Similar to Figure 5.6, Figure 5.7 shows the results for the PD distributions for simulated gamma-rays from a source of spectral index $\Gamma = 2.6$. For this, the same number of events were simulated and in Figure 5.7a, the distribution of events that survived shape cuts (13,220) can be seen, although only 10,004 events could be reconstructed with CT5. Figure 5.7b is Figure 5.7a with two filters applied, i.e. a minimum of two telescopes required and only mono-reconstructed events considered. This plot has 5,400 events that survived the filters. This means that 5,400 events that could be reconstructed with CT5 triggered at least two telescopes. As a percentage of all events, this is 0.8%, yet more than enough to give a comfortable excess that may survive MSSG cuts as evidenced in Figure 5.7c, which has 4,596 events. Figures 5.7c and 5.7d show the distribution of these events with the standard PD selection cuts in red. A consistent feature of both simulations is that a reduction in the lower limit of

PD to $\simeq -2$ could considerably ameliorate the gamma rays surviving. This is perhaps seen more clearly in Figure 5.8 where the Crab Nebula data set is compared to the two simulations. The Crab Nebula data resembles that of the simulations at low PD values and deviates drastically at the higher PD. The cut performed on this variable clearly disregards a large number of photons and considers them as background.

Hadron Simulations

For background, protons were simulated, with telescopes pointing $180°$ south w.r.t. H.E.S.S., a zenith angle of $18°$ and a source with a spectrum obeying a power law of index $\Gamma = 2.4, 2.6$. An off-axis angle of $0°$ is used for the hadron simulations, as opposed to the $0.5°$ used for the photon simulations, so as to get a better statistic (a histogram with more events) after shape cuts. Statistically, most hadron induced events can be rejected by the shape cuts.

The simulations in general show that the shape cuts remove the majority of the background events. For a proton source of spectral index of $\Gamma = 2.4$, 248,529 events were simulated and only 301 survive the shape cuts (Figure 5.9a). That is a little over 0.1% of all the proton simulations that survive in this data set. From 301 events, 279 could be reconstructed with CT5 and 153 of these triggered a second telescope. Figure 5.9b shows their distribution. Perhaps most interestingly, after performing the standard MSSG cuts, only 66 events survive and many of them are accepted as false positives by the standard PD cuts (see Figure 5.9c). Adding two more false positives by decreasing the lower limit to $-2X_0$ would allow for a larger excess while not affecting the false positive rate significantly.

The same result is predicted by the simulations of protons from a source of spectral index $\Gamma = 2.6$. Figure 5.10 shows these results, where Figures 5.10a and 5.10b generally have more events because for this Γ more showers were simulated, exactly 881,040. This is far more events than previously, however, the PD essentially follows

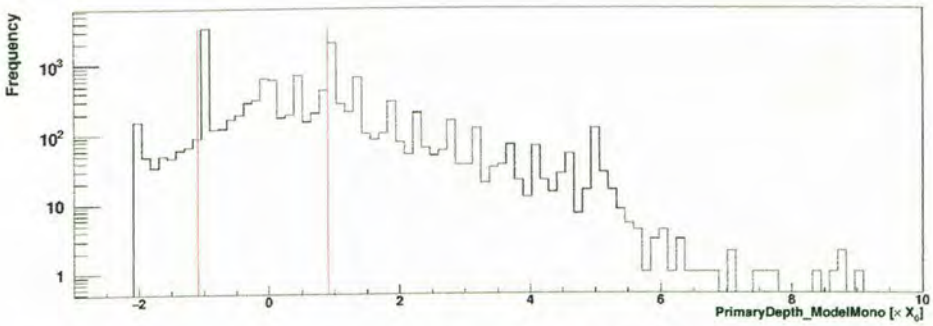

(a) PD distribution for events that could be reconstructed with CT5 alone, with no $PD = -1X_0$ filter applied. This histogram has 13,220 events that have been reconstructed and a logarithmic frequency scale. The reconstruction failed for 3,216 events which gives the rise to the peak at $-1X_0$. The red lines show where the PD cut will be applied.

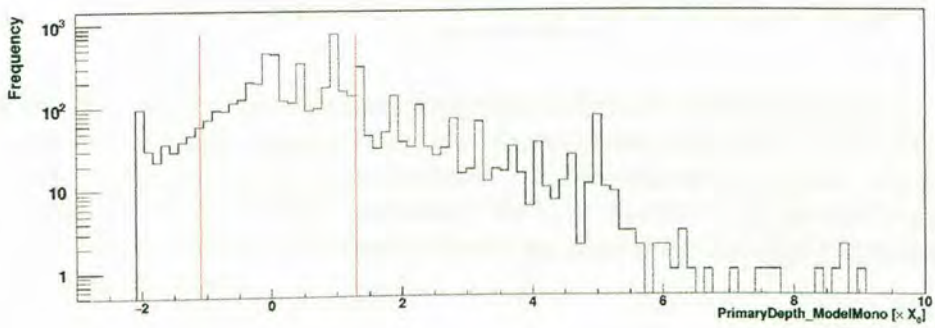

(b) PD distribution for mono-reconstructed events that have triggered more than one CT. Here a filter has now been applied to remove the 3,216 events that failed to be reconstructed and to remove events that only triggered one telescope. In this histogram is seen 5,400 events and in red the cuts to be applied to this variable.

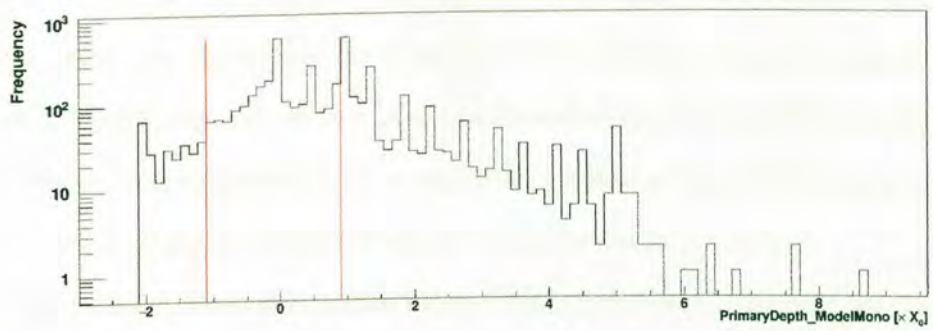

(c) PD distribution for mono-reconstructed events with one more filters applied, the MSSG cut. In this histogram is seen 4,596 events, meaning 804 events could not survive the MSSG cut. Standard cuts to the PD are shown in red.

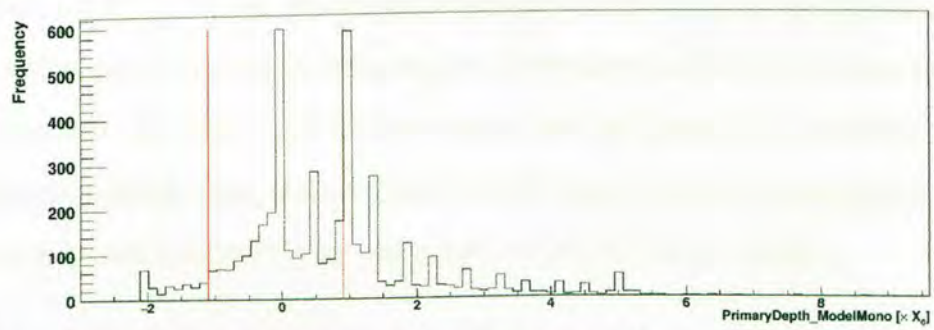

(d) PD distribution for mono-reconstructed events triggering two telescopes and passing MSSG cut criteria, with frequency not logarithmic. Standard cuts to the PD are shown in red.

Figure 5.7: Results for $\Gamma = 2.6$ spectral index photon source simulations. Here c) and c) are the contain the same data but different y-axis scales.

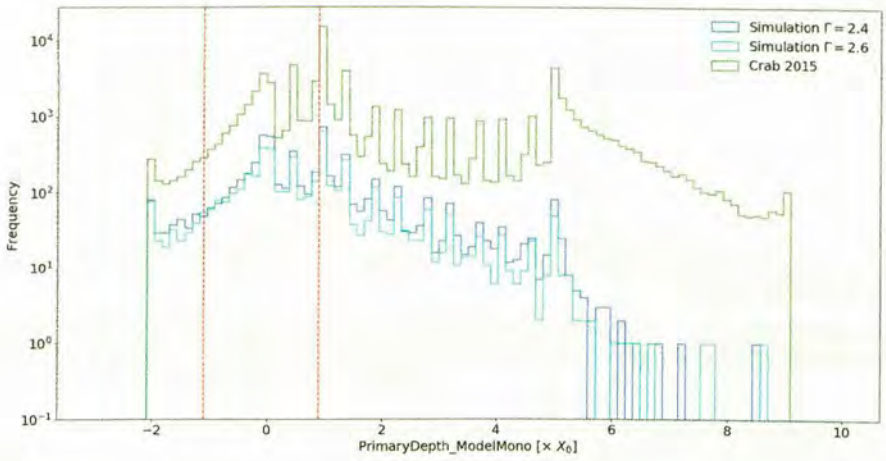

Figure 5.8: Primary Depth histogram in log scale of the Crab Nebula data set (green) and the two photon simulations (cyan and blue). The blue histogram is for the $\Gamma = 2.4$ simulation of gamma rays and the cyan histogram for the $\Gamma = 2.6$ gamma ray simulations. The red lines show where the PD cut would be performed. The Crab data set has many more entries in its histogram because there are more events however, the shape is similar to that of the simulations except for the PD $> \simeq 5$.

the same distributions. Figure 5.10a proves that 0.08% of the events survive the shape cuts as it only has 703 entries. Furthermore, cuts on the showers that could not be reconstructed and in addition the lower limit of 2 telescopes triggered, results in 348 events still surviving. All but one peak is removed by the standard MSSG and PD cuts and, similar to the previous case, a negligible number of excess events are added as false positives if the lower limit of the PD cut is moved to $\simeq -2X_0$.

Figure 5.11 is a visual representation of the simulations at different spectral index (Γ). It Illustrates how many hadrons would be accepted as signal if the PD cut is moved to $PD = -2\,X_0$. The standard analysis takes the range of the highest number of photon induced events in the histogram, unfortunately adding the largest range of Hadron induced events. This is more clearly seen in Figure 5.11b where the highest frequencies clearly occur in the accepted events. Figure 5.11 also illustrates how much signal is gained compared to the added false positives. This is negligible.

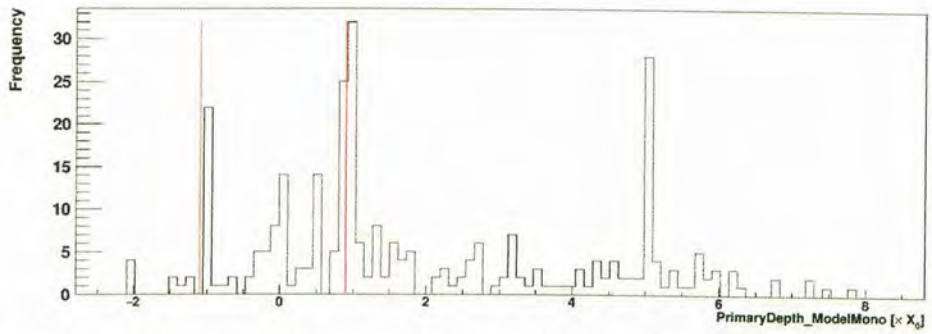

(a) PD distribution for events that could be reconstructed with CT5 alone, with no $PD = -1X_0$ filter applied. This histogram has 301 events that have been reconstructed. The reconstruction failed for 22 events which gives the rise to the local maximum at $-1X_0$. The red lines show where the PD cut will be applied.

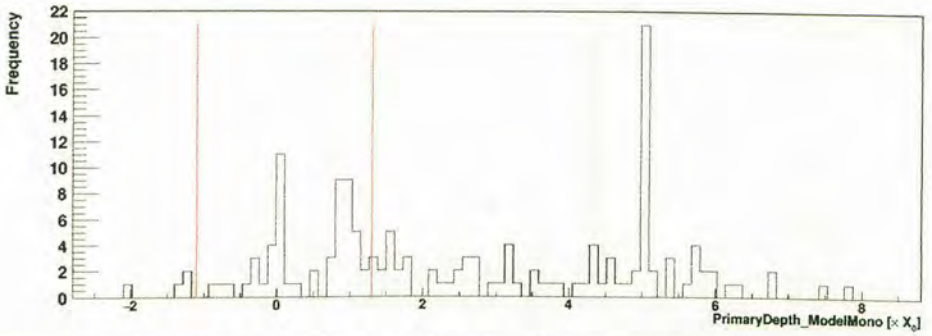

(b) PD distribution for mono-reconstructed events that have triggered more than one CT. Here a filter has now been applied to remove the 22 events that failed to be reconstructed and to remove events that only triggered one telescope. In this histogram is seen 279 events and in red the cuts to be applied to this variable.

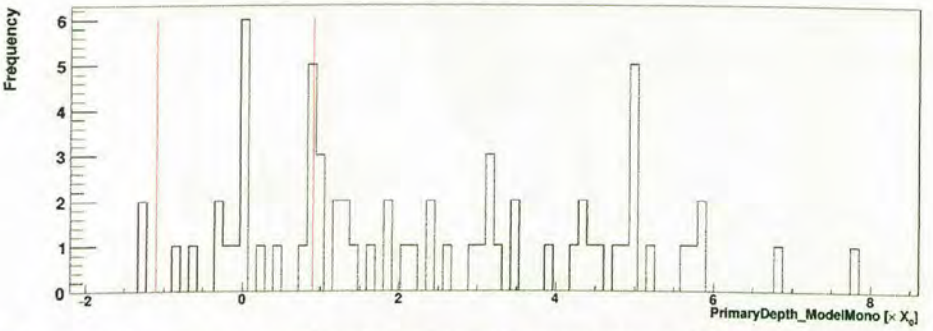

(c) PD distribution for mono-reconstructed events triggering two telescopes and passing MSSG cut criteria. Standard cuts to the PD are shown in red. This histogram has only 66 events.

Figure 5.9: Results for $\Gamma = 2.4$ spectral index hadron source simulations.

5.3 Adjusted PD cut application

As suggested in Section 5.2, a new cut was applied to the PD separation variable in a new Crab Nebula mono-analysis of the same data used in Section 5.1. This was done to test it's performance of this new cut. Figure 5.12 presents the θ^2 distributions for the standard analysis and that for the adjusted PD cut with some statistics from the analysis. The standard analysis results in a $58.5\ \sigma$ detection significance with a signal

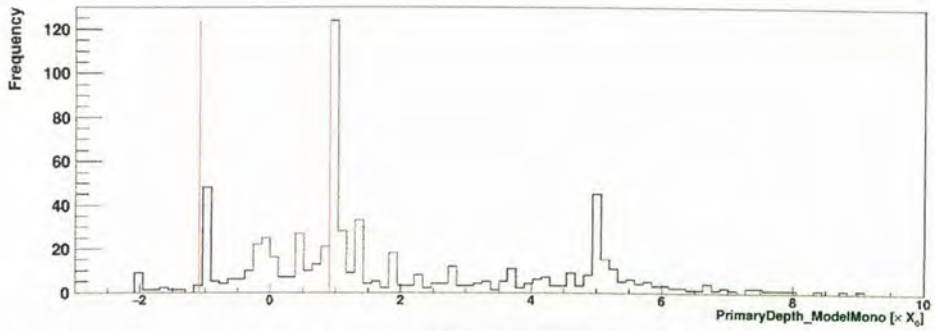

(a) PD distribution for events that could be reconstructed with CT5 alone, with no $PD = -1X_0$ filter applied. This histogram has 703 events that have been reconstructed. The reconstruction failed for 47 events which gives the rise to the local maximum at $-1X_0$. The red lines show where the PD cut will be applied.

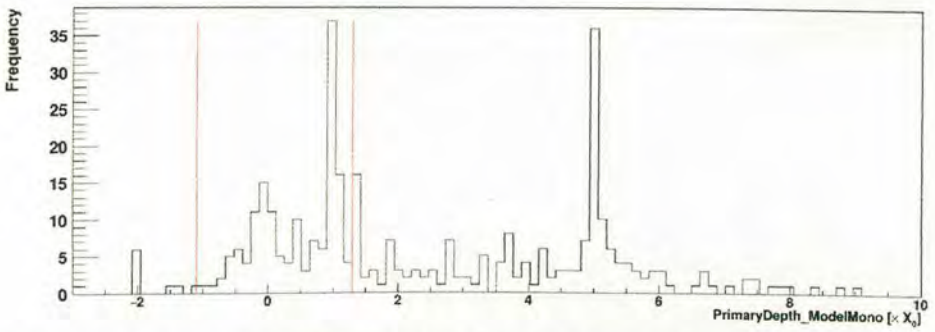

(b) PD distribution for mono-reconstructed events that have triggered more than one CT. Here a filter has now been applied to remove the 47 events that failed to be reconstructed and to remove events that only triggered one telescope. In this histogram is seen 348 events and in red the cuts to be applied to this variable.

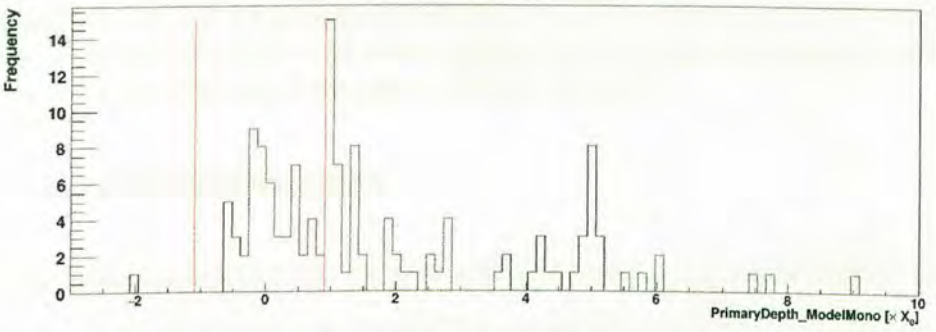

(c) PD distribution for mono-reconstructed events triggering two telescopes and passing MSSG cut criteria. Standard cuts to the PD are shown in red. This histogram has 134 events.

Figure 5.10: Results for $\Gamma = 2.6$ spectral index hadron source simulations.

to noise ratio of 9.3. Adjusting the lower PD cut to $-2X_0$ results in an increase in the detection significance by 1.1 σ while decreasing the signal to noise to 9.2. With these results, it is clear that the new cut performs better than the standard analysis as the signal to noise remains in its error limits.

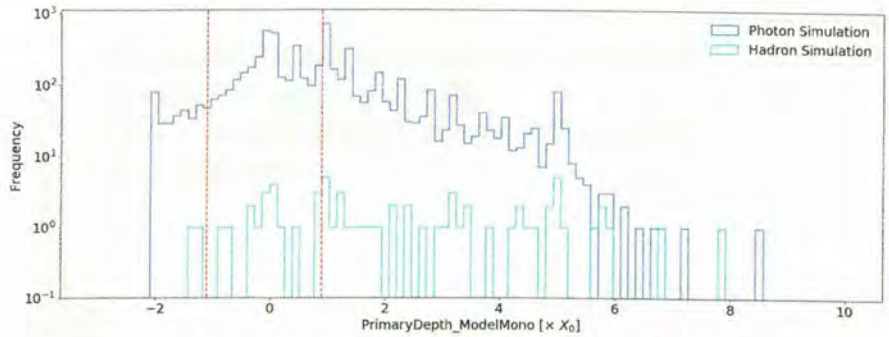

(a) Simulations of photons and hadrons from a source of $\Gamma = 2.4$

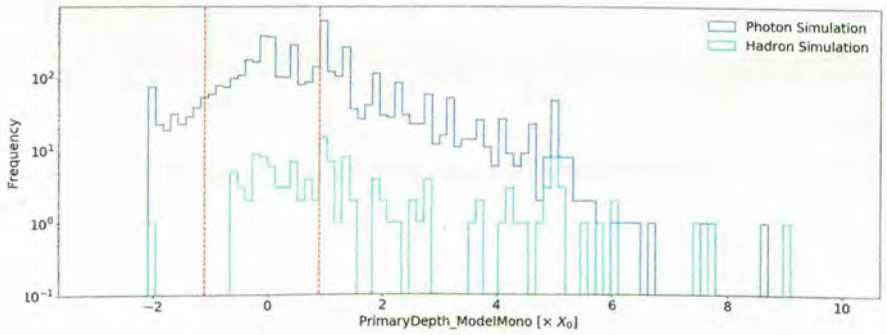

(b) Simulations of photon and hadron from a source of $\Gamma = 2.4$

Figure 5.11: Different spectral index simulations of photons and hadrons. a) Illustrates how the photon simulation (blue) compares to the hadron simulations (cyan) when a source with a spectral index of $\Gamma = 2.4$ is simulated and b) shows the same for a source of $\Gamma = 2.6$. At this point of the analysis a very small number of hadrons still remain. The photons remaining are of the order 10^2 while that of the hadron are of the order 10^0.

5.4 Cross-Correlation studies

In this section results for the multi-wavelength time lag (hereafter referred to simply as lag) studies are presented. For all lag calculations made, the convention of radio emission lagging X-rays or gamma-rays is used. This is done as it is known that the jets of micro-quasars culminate in radio lobes [22].

Confirming 2018 results

To confirm that the method is well understood, the newly developed code[2] that was written in python for cross-correlations was used to reproduce 2018 results of [49]. Figure 5.13 shows results of this work in comparison with that presented in 2018.

[2]Code available at https://github.com/ShapopiJ/Cross-Correlation-Code.

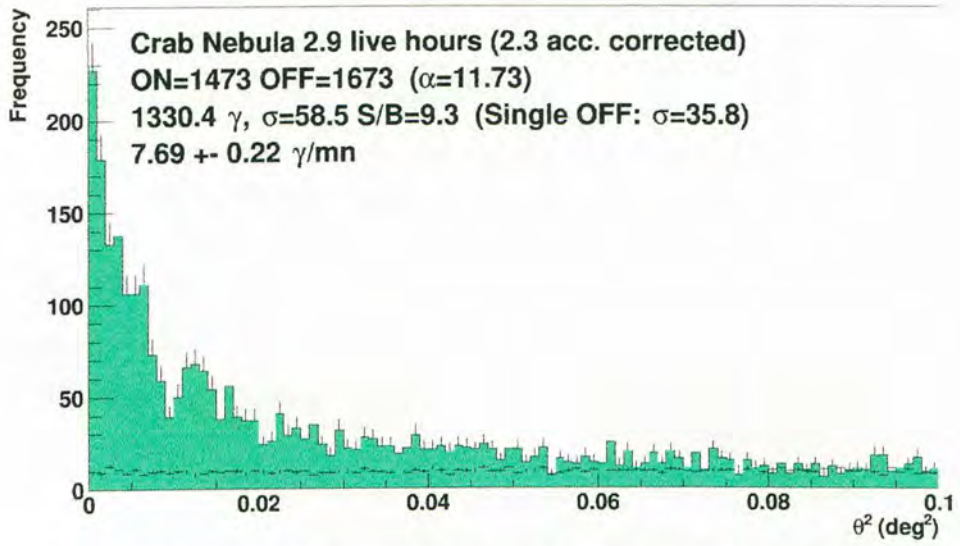

(a) Theta squared plot for the standard analysis with the PD distribution cut set to $-1.1 \leq PD \leq 1.3$.

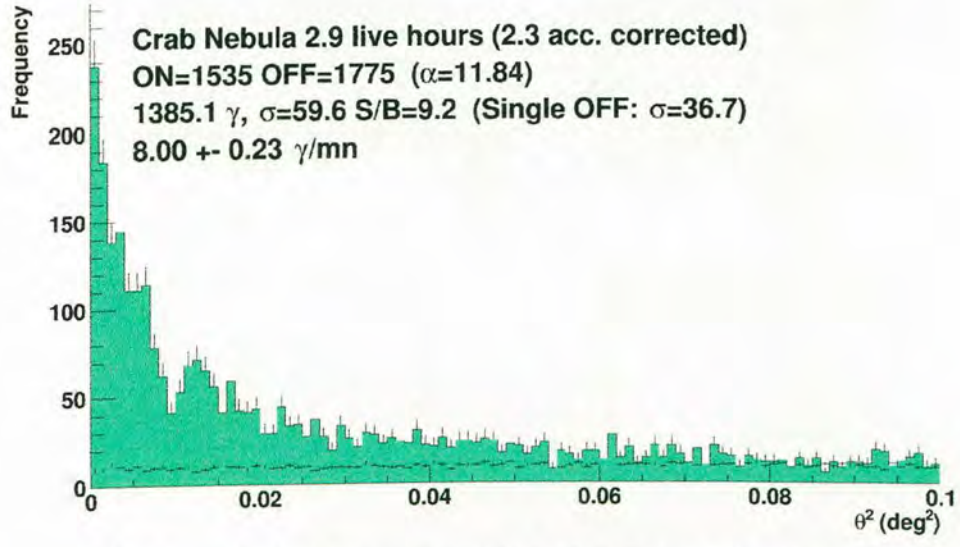

(b) Theta squared plot for the standard analysis with the PD distribution cut set to $-2.0 \leq PD \leq 1.3$.

Figure 5.12: The optimized analysis b) performed better than the standard mono-analysis a) gaining a 1.1 σ significance.

Unsurprisingly the plots are almost identical to one another. This was unsurprising because the same method was used only with different programming languages and this could be the reason for discrepancies found in results at orders of 10^{-4}.

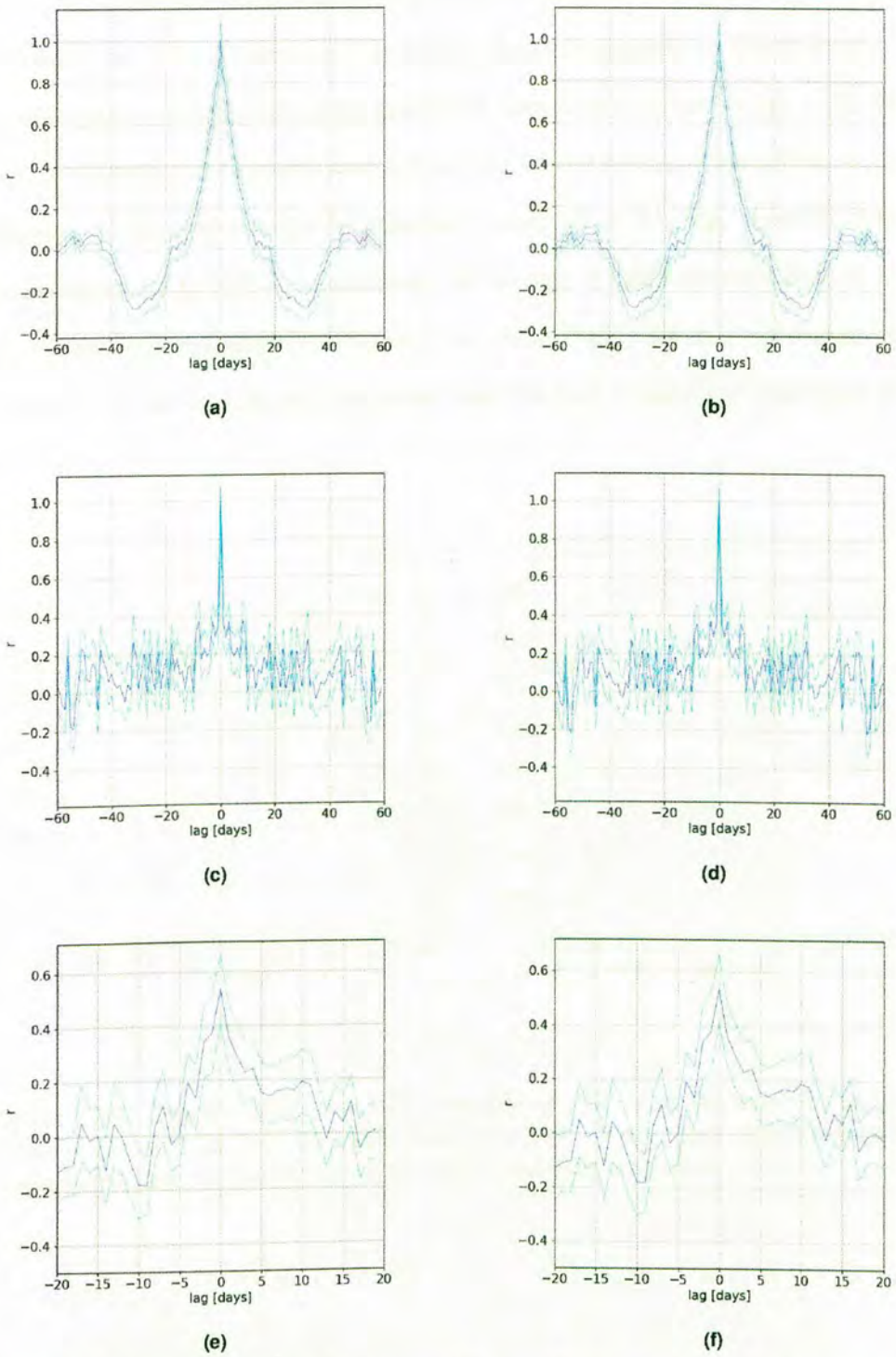

Figure 5.13: Results for auto and cross-correlations of 1 day binned 15GHz, gamma-ray and X-ray data from Cyg X-3. a), c) and e) are results for the program written in this work and b), d) and f) are the results presented in [49]. a) and b) are the auto-correlations of radio data, c) and d) the auto-correlations of the gamma-ray data and e) and f) the cross-correlation of gamma-ray and 15 GHz data. For all plots, blue is the correlation and cyan the error on the correlation.

Figures 5.13a, 5.13b and 5.13c, 5.13d show results for the auto-correlation of 15GHz radio and gamma-ray data, respectively. As these are auto-correlations it is expected to have a peak at $r = 1$ for $x = 0$ and have identical shapes on either side of $x = 0$. The discrepancy mentioned earlier is perhaps best seen at values of lag $\simeq 55$ days in the auto-correlation of gamma rays (Figure 5.13c and 5.13d), where there is a slight difference in the anti-correlation minimum observed at this lag. Perhaps the most interesting results in [49] is the discovery of the lags of radio emission behind X-rays. These results are reproduced in Figure 5.14a, while Figure 5.14b is the original result. In conclusion, the code is well suited to study the lags in the same data types of Cyg X-1.

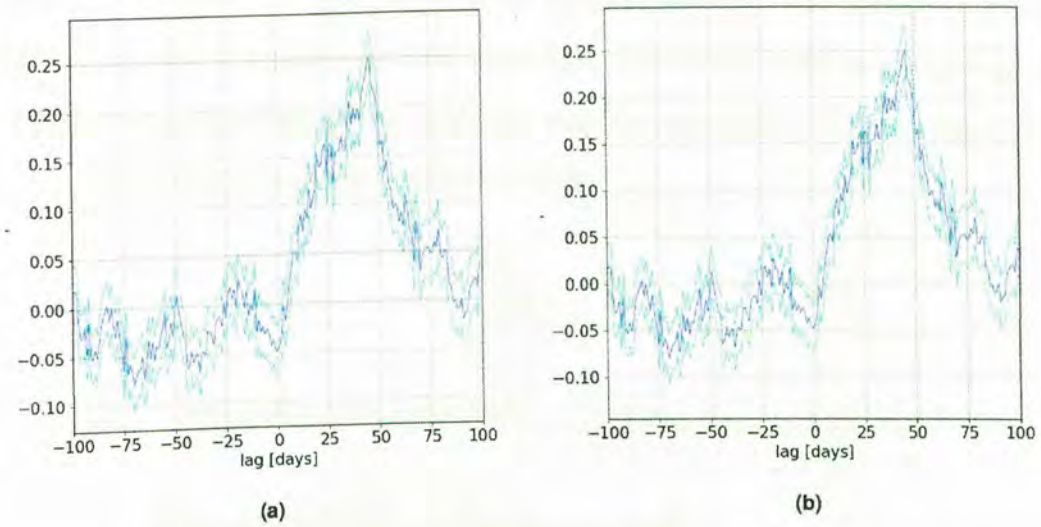

Figure 5.14: Cyg X-3 X-ray and radio correlations [49]. a) is the result for the program written in this work and b) is the result presented in [49]. A clear peak of 0.25 is seen at ~ 44 days in both a) and b). The blue is the correlation and cyan is its error.

5.4.1 Cyg X-1 Cross-correlation studies

With the confirmation of the 2018 results from [49], the method was validated and the results of further applications are reliable. Relevant and interesting results for the Cyg X-1 data sets are presented. In this work no auto-correlations have been considered as they do not provide us with information about the lag of radio waves behind X-rays. The un-binned/original data changed little to nothing in all plots, the most notable change being the smaller error margins, and was only considered in some cases. Visualized light curves are presented before correlations.

ASM vs 15 GHz

Figure 5.15 provides the light curves of the 15 GHz radio data and the 1.5 – 12 keV ASM X-ray data. The large gap in the radio light curve is due to the re-configuring of the Ryle telescope to become the AMI large array between 2006 and 2007. The ASM X-ray data also has a large gap at MJD $>$ 56000.

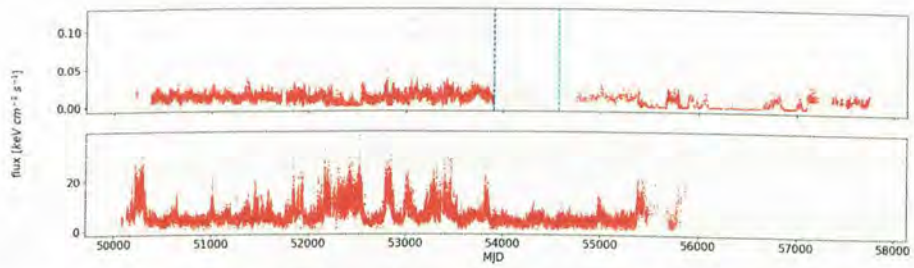

Figure 5.15: Light curves of the radio and ASM data. At the top is seen the light curve of the radio data in red. There is a very large gap in the data from 53905 MJD (blue stripped line). This is when the Ryle Telescope was switch off and in cyan is seen when the AMI began operations. Much less measurements of Cyg X-1 were made with AMI than with the Ryle telescope on a daily basis. The bottom figure contains the light curve for the ASM data in the 1.5 – 12 keV energy range.

Data from the ASM was cross-correlated with 15 GHz emissions from Cyg X-1. Figure 5.16a shows results for the cross-correlation of 1.5 – 12 keV and 15 GHz Cyg X-1 data, i.e. the sum of all energy bands available in the ASM data set. The sum of all energy bands here, is considered as all photons that have been detected with an

energy between 1.5 – 12 keV. The data was split into hard/intermediate and soft dates in accordance with the dates given in Table 4.2. Figure 5.16a is the result for the hard/intermediate state of the source and Figure 5.16b for the soft state.

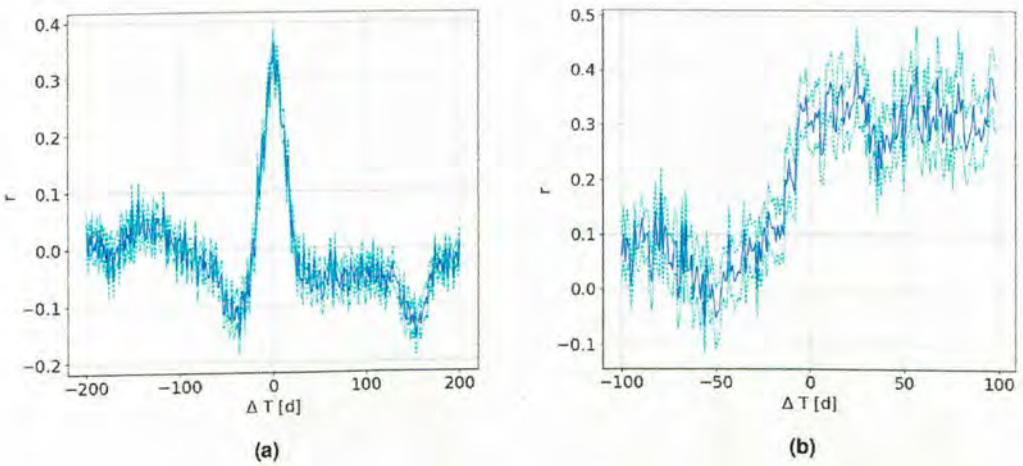

Figure 5.16: Cyg X-1 X-ray and radio correlations for 1.5 – 12 keV, where a) is the correlation in the hard/intermediate state and b) that in the soft state of Cyg X-1. The blue is the correlation and cyan is its error. A clear peak is seen in a) the hard/intermediate state suggesting a strong correlation between the X-ray and radio emission in this state. In the soft state a) the correlation is too large a range to confidently there is a lag (or lack there of).

In the hard state, the data is well correlated at 0 lag and all energy bands give a characteristic peak at 0 lag (see appendix C for hard state correlations in different energy bands). In the soft state, however, there is no clear peak of correlation, yet the correlation does increase above zero lag and remains high. To gain deeper understanding, the data was split into their different energy bands and studied for lags. In Figure 5.17 are the results for the soft state cross-correlation in the different energy bands. There is some evidence of lags in softer X-rays < 5 keV as seen in Figure 5.17a and 5.17b. The peak is seen at a lag of about 140 days. However, as the energy increases the peak disappears. This evidence can be seen in Figure 5.17c, which shows harder X-rays of the 5–12 keV correlation. This plot rather takes on a shape similar to that seen in the hard state correlations of Cyg X-1.

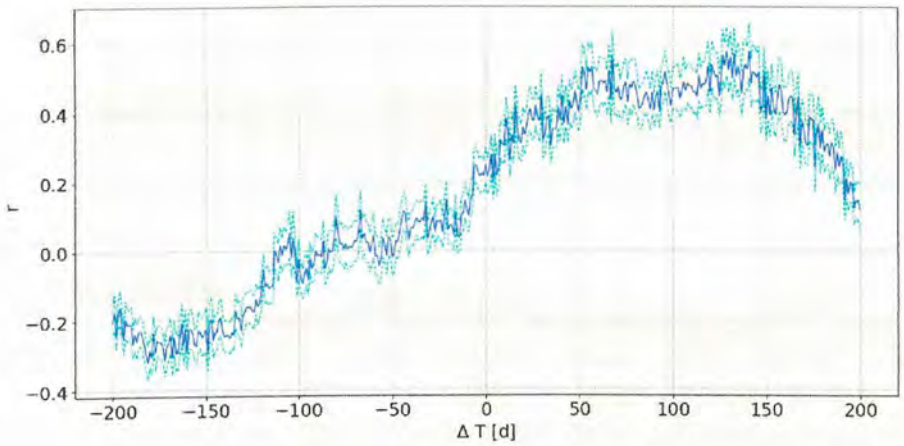

(a) 1.5–3 keV.

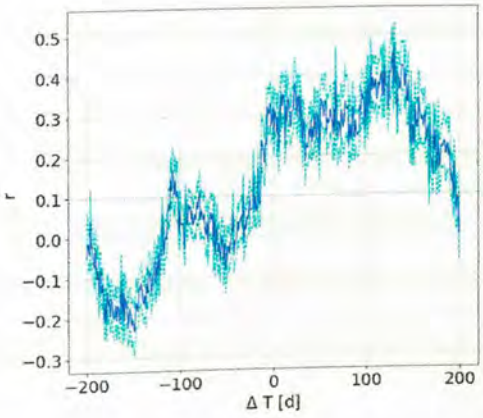

(b) 3–5 keV.

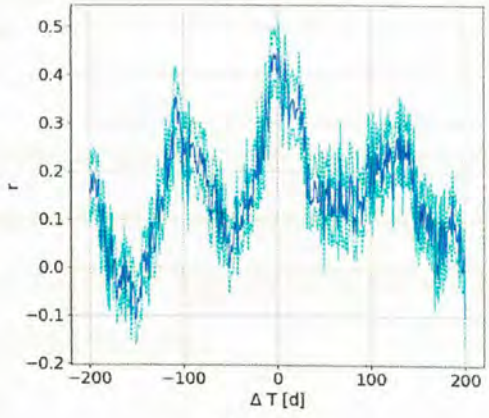

(c) 5–12 keV.

Figure 5.17: Cross-correlations of different X-ray bands vs. 15 GHz radio emission in the soft state Cyg X-3. The blue is the correlation and cyan is its error. a) shows the correlation in the 1.5 – 3 keV band and gives some evidence of lag in a wide range of days 100 – 150 days. This evidence is also slightly visible in b) which shows the correlation with of the 3 – 5 keV band. c) shows the correlation of the 5 – 12 keV band, and in it the evidence of previous lags is diminished. There is a peak at in the correlation at 0 days.

MAXI vs 15 GHz

Cross-correlations of MAXI X-ray data with radio data had an underlying problem that there were too many gaps in the light curve for X-ray data. Figure 5.18 shows the LCs from MJD 55000 to 57000 for the MAXI (top) and BAT (bottom) data. In comparison to the BAT data, the MAXI data has far too many gaps. These gaps will affect results in ways not understood at this stage.

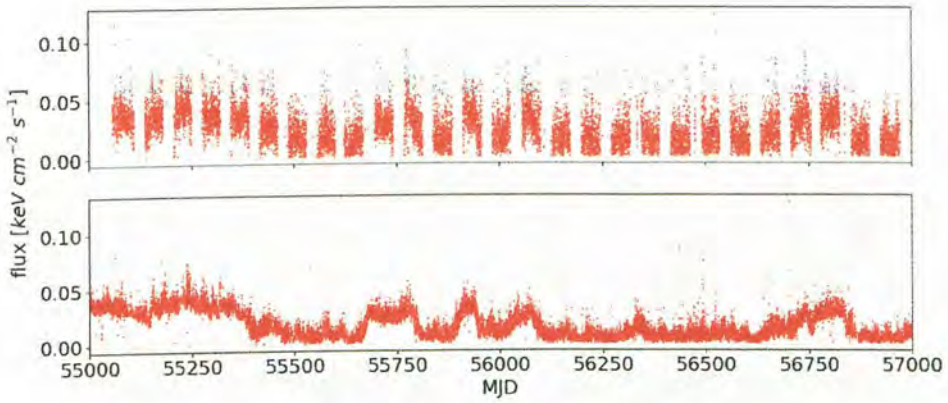

Figure 5.18: Un-binned raw light curves for MAXI data in comparison to that of BAT for 2000 days. At the top is the MAXI light curve and at the bottom the BAT light curve. The MAXI light curve exhibits periodic gaps in data while the BAT light curve has very little negligible gaps, e.g. between 56750 – 57000 MJD. The effect these gaps have on the cross correlations are not well understood at this stage.

For these cross-correlations only the finely resolved data sets were used as opposed to the 1 day binned method in an effort to remove some sources of errors. Figure 5.19 shows the results for the sum of all bands i.e. 2 – 20 keV (Figures 5.19a, 5.19c, 5.19e) and the c band i.e 10 – 20 keV (Figures 5.19b, 5.19d, 5.19e).

Similar results are obtained for the bands: 2 – 4, 4 – 10, 2 – 20 keV. All of these exhibit a peak at $\Delta T \simeq 110$ days. Figure 5.19a is inserted as a representative of the rest, which can be seen in appendix C. This is split into the hard and soft state durations in Figures 5.19c and 5.19e, respectively. The peak is then maintained in the hard state but seems to be periodic. There is however a clear and consistent anti-correlation before the peak at 110 day lags. This peak is also seen in the 2 – 20 keV hard state correlation (Figure 5.19d) and is non existent in the soft and combined state correlations (Figures 5.19f and 5.19b, respectively).

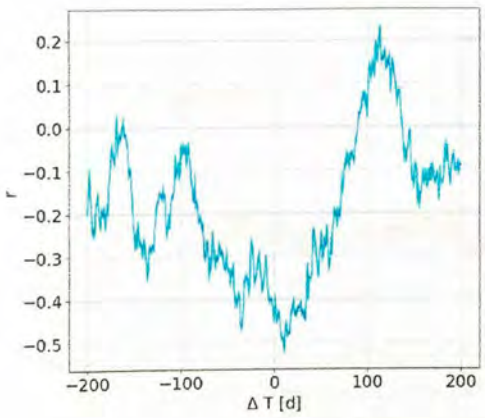

(a) 2 – 20 keV in all states

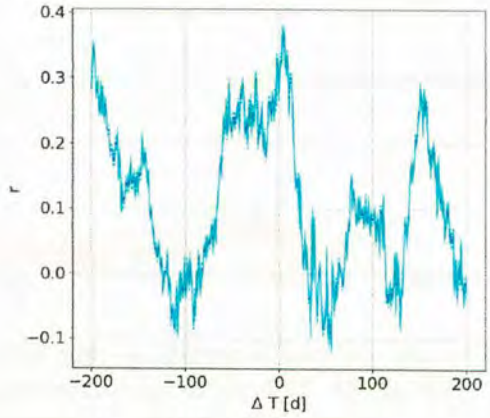

(b) 10 – 20 keV in all states

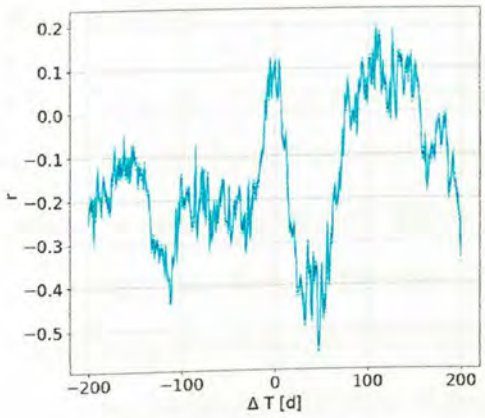

(c) 2 – 20 keV in hard state

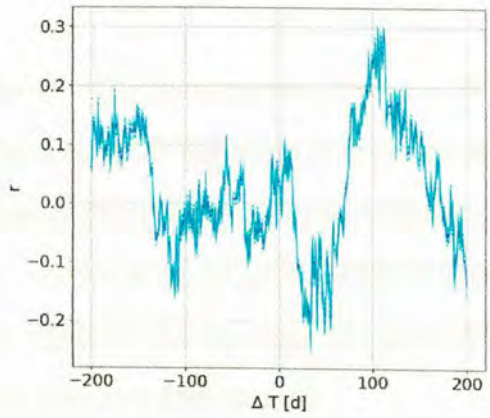

(d) 10 – 20 keV in hard state

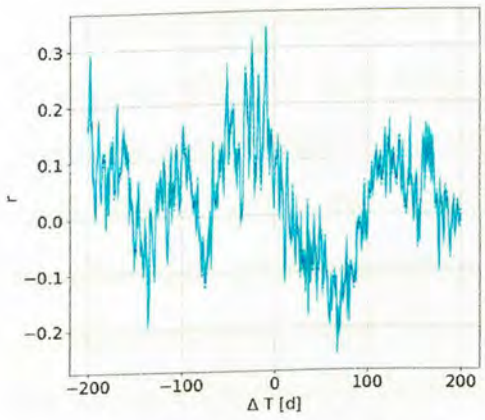

(e) 2 – 20 keV in soft state

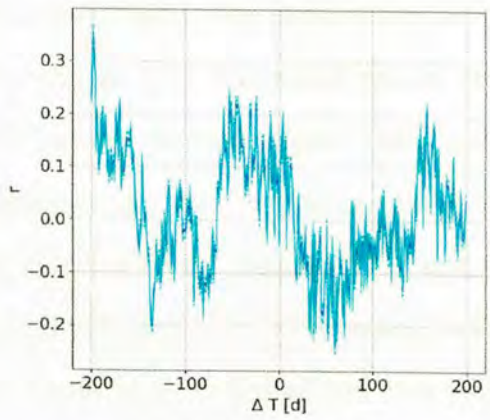

(f) 10 – 20 keV in soft state

Figure 5.19: Results for auto and cross-correlations of un-binned 15GHz with, MAXI data in 2 – 20 keV range (a, c and e) and 10 – 20 keV (b, d and f) in different states of Cyg X-1. The blue is the correlation and cyan is its error. a) shows a peak of 0.2 at ∼100 days. Using higher energies gives no unique peak of correlation, as seen in b). In the hard state the the 2 – 20 keV correlation (c) shows more anti-correlation than correlations. At higher energies (d) the hard state correlation has a peak at ∼100 days. The soft state correlation e) and f) show no clear correlations either.

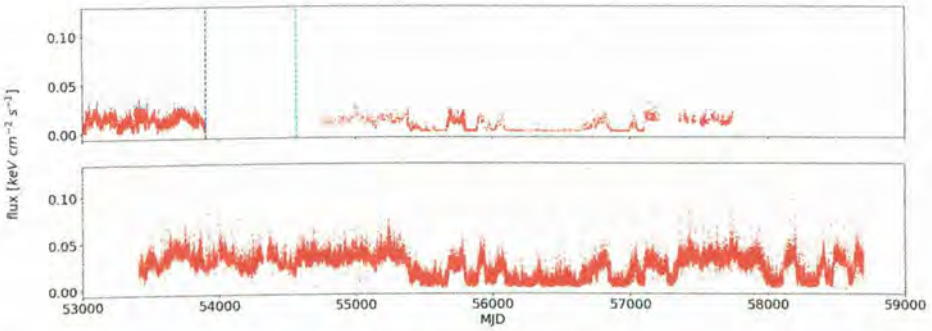

Figure 5.20: Light curves of the radio and BAT data. At the top is seen the light curve of the radio data in red. The colors have the same meanings as that in 5.15. The bottom figure contains the light curve for the BAT X-ray data in the 15 – 50 keV energy range.

BAT vs 15 GHz

Figure 5.20 provides the light curves of the 15 GHz radio data and the 15 – 50 keV BAT data. This figure is focused on the BAT data as the full range of the radio data is already shown in Figure 5.15. Figure 5.20 illustrates that the X-ray data taken here is more consistent than all the other X-ray sources with no gaps visibly appearing. When compared to the 15 GHz radio data, the BAT data has only 281 days with no data compared to the 3983 days of the entire Ryle and AMI data set.

This data has a single energy band which is 15 – 50 keV. Thus these results are radio correlations with very hard X-ray data. Figure 5.21 shows the results of this correlation un-split (Figure 5.21a) and split between the hard (Figure 5.21b) and soft states (Figure 5.21c). The un-split correlation presents surprising results when compared to the soft state correlation. It is expected for the correlation for hard states to have a lower peak, however, the results seen in Figure 5.21c is interesting, as this is the state in which the radio emission flux would be at its highest and thus a higher peak for the cross-correlation coefficients was expected. It is however reduced by as much as $r \simeq 0.3$.

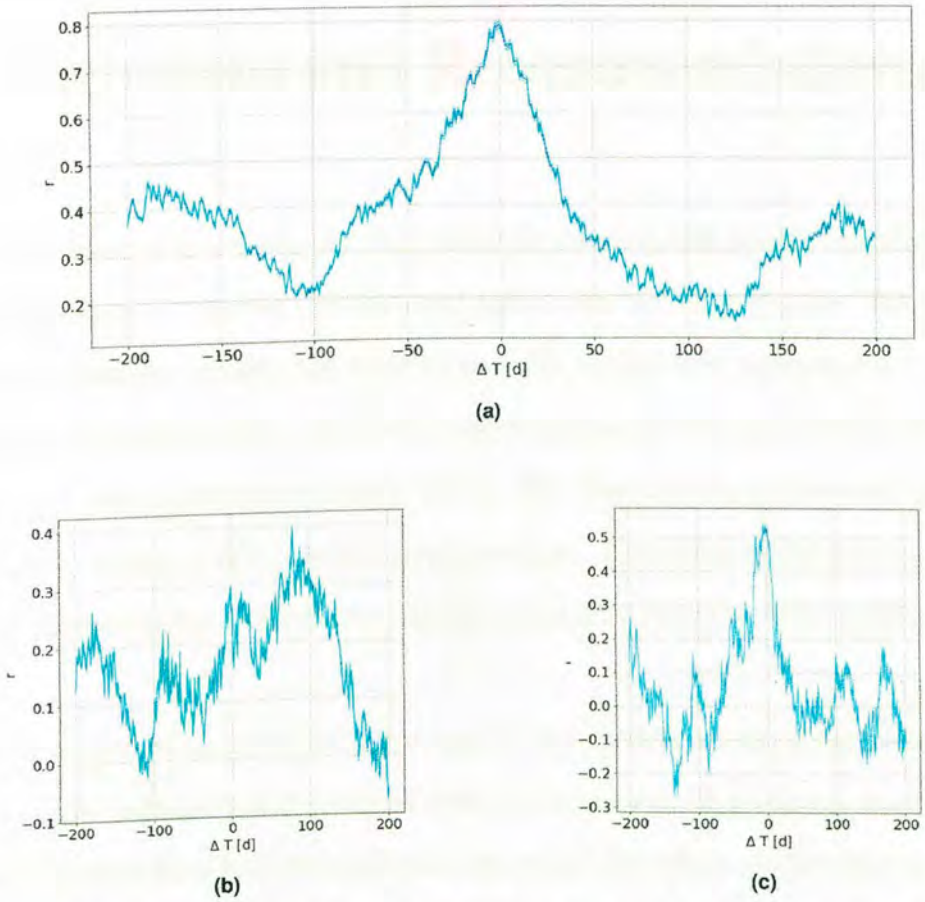

Figure 5.21: Correlations of 15 – 50 keV with 15 GHz in different states of Cyg X-3. a) is the un-split/combined correlation, b) the correlation of data taken in the hard state and c) that of the hard state of Cyg X-3. The blue is the correlation and cyan is its error. In b) is seen a range of possible lags, ~50 –110 days. In a) and c) is seen that the combined state has a higher peak than the soft state.

Chapter 6

Conclusions and Recommendations

In the context of this thesis, the Paris Analysis software was installed on the HPC at the University of Namibia and was cross tested with two other clusters. The primary depth separation variable has been extensively studied and optimized for a more robust yet sensitive result. The most consistent result for the optimization of the PD cut was to reduce the lower limit to $-2X_0$. This increases the excess while adding a minimal amount of false positive reconstructions. Compared to the already existent false positives in the standard analysis, the added false positives are insignificant.

The reduction of the lower limit was applied and produced a more significant result. The results, however positive, are not without uncertainty. To produce a more realistic result, it might be of interest to calculate the probability of two muons striking the two CTs at the same time. This may remove doubts of the assertions that any particle that triggers more than one CT is not a muon. In addition, simulating different off-axis angles will grant a more stable result, as this is an uncertainty not well handled in this work. Different off-axis angles could be simulated and their different suggested cut optimizations integrated to give a more general result that can be applied to all sources. In addition, the new PD cut was only applied to the mono-analysis without considering the number of telescopes triggered for the added events below $-1.1\ X_0$. This is important as the PD analysis was done under the assumption that more than one telescope was triggered. Once this multi-trigger is taken into consideration, the

new mono-analysis can then be integrated into the combined analysis.

The 15 GHz radio data was correlated with X-ray data of different bands in search of time lags. The time lag results, seen with the ASM data, in soft state of Cyg X-1 is interpreted as the time taken for magnetic field advection from the donor star to the accretion disk.

To get more statistically accurate results, the gaps in the LC data from MAXI need to be considered. Assuming the results are roughly accurate, the lag of 110 days characteristic to the soft state of Cyg X-1 in all energy bands could be caused by the same reason as that described for ASM data. Advection of the magnetic field takes some time. The peak is observed at around the same position within the range 110 – 140 days, although it does not appear in the 5 – 12 keV energy band. What can be said with some certainty is that radio emission lags soft X-rays by an order of 10^2 days. The strong correlation of 15 – 40 keV with 15 GHz radio emission is evidence of the jet production being directly driven by the hot, hard X-ray emitting, corona through all spectral states of Cyg X-1. These results can be used to study Quasars that accrete mass from their host galaxies. This work lays some ground work for this application and the improvement of the H.E.S.S. mono analysis plays an important role.

Appendix A

Standard Model

This section provides some introductory background to the standard model of particle physics. The standard model is a theory of fundamental particles and unites three of the four known fundamental forces (Strong and Weak nuclear forces and Electromagnetic force) [13]. There are 30 named particles in the standard model. These particles can be seen in Figure A.1, which shows all the particles grouped in their respective classes, i.e leptons, quarks and bosons. Leptons and quarks belong to another family called fermions[1].

Table A.1 outlines some properties of the particles, masses, spins, charges, etc. The most recently discovered particle is the higgs boson, which was detected in 2012. In Table A.1, the colors of different quarks and gluons can be seen. The colors of quarks have no relationship to the visible wavelength colors. Rather, these colors are names given to the quarks of different "flavors" that interact in the strong nuclear force. The quark colors are red, green and blue and their anti-quarks have anti-colors. No other color quarks exist. Gluons come in 8 different colors which are combinations of the quark and anti-quark colors. The gluon is the particle exchanged by quarks responsible for their strong nuclear interaction. All quarks and leptons have accompanying anti-particles with opposite charges, e.g. the electron e^- has a positron e^+ as its antiparticle, which has the same mass. For neutrinos, only upper limits to

[1] named after Enrico Fermi [12]

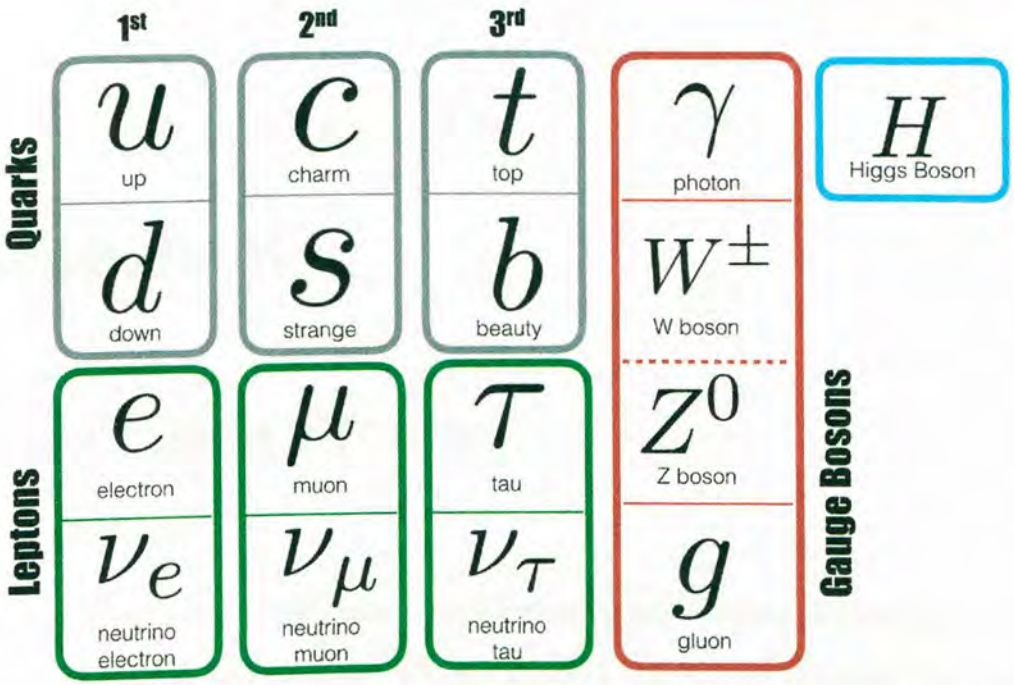

Figure A.1: Tabular view of particles predicted by the standard model grouped in their classes [59]. The beauty particle is more often called "bottom".

particle	prediction	dicovery	spin	charge (e)	color	mass (MeV/c^2)
up quark (u)	1964	1968	1/2	+2/3	r, g, b	4.67
down quark (d)	1964	1968	1/2	-1/3	r, g, b	4.67
charm quark (c)	1970	1974	1/2	+2/3	r, g, b	1,270
strange quark (s)	1964	1968	1-2	-1/3	r, g, b	93
top quark (t)	1973	1995	1/2	+2/3	r, g, b	172,900
bottom quark (b)	1973	1977	1/2	-1/3	r, g, b	4,180
electron	1874	1897	1/2	-1	none	0.51099895
muon (μ)		1936	1/2	-1	none	105.658375
tau (τ)		1975	1/2	-1	none	1776.86
electron neutrino (ν_e)	1930	1956	1/2	0	none	$< 2 \cdot 10^{-6}$
muon neutrino (ν_μ)	1940s	1962	1/2	0	none	< 0.19
tau neutrino (ν_τ)	1970s	2000	1/2	0	none	< 18.2
gluon (g)	1962	1978	1	0	8 colors	0
photon (γ)		1899	1	0	none	0
W boson	1968	1983	1	± 1	none	80,379
Z boson	1968	1983	1	0	none	91,187.6
higgs boson	1964	2012	0	0	none	125,100

Table A.1: Overview of particles predicted by the standard model [12]. Particle charges are given as factors of the elementary charge $e = 1.6021 \cdot 10^{-19}$C. The colors r,g,b are red, green and blue, respectively. Mass is given in terms of their rest mass energy divided by the speed of light.

their masses have been established.

Appendix B

Installation Process

The installation process, although straight forward, can be arduous depending on the subject system. In the case of the HPC at UNAM, CentOS 7 was installed. This was in an effort to duplicate as much as possible the system at the University of Witwatersrand (Wits).

ROOT was downloaded from the CERN website. To find out the missing dependencies, the script "configure" was executed while inside the ROOT directory[1]:

```
./configure linuxx8664gcc --all  --enable-tmva --enable-genvector --
    enable-cintex --enable-reflex  --enable-minuit2 --enable-xml
```

The output is a list of all dependencies and their status of installation. The libraries that were missing were all installed. A list of all additional libraries installed and their descriptions can be found in Table B.1. After all libraries and dependencies were installed, ROOT was built using the make utility, which makes building executable files from source code easier. It generally contains rules for building the executables. AstroROOT was built in a similar fashion.

For the graphical user interfaces, "gtkextra" had to be installed. To do this, the Red Hat Package Manager[2] (RPMs) had to be rebuilt from source packages.

[1] this is ROOT version 5.34.36

[2] this is the equivalent of a .deb file for Ubuntu or .exe for Windows.

Table B.1

Library	Purpose
cfitsio	Library for fortran and C providing simple high-level routines for reading and writing image files in the Flexible Image Transport System (FITS) format
mariadb	Open source database server
gsl gsl-devel	GNU Scientific Library
fftw	Fast Fourier Transform in the West. It is a library for performing discrete FFTs
ruby	A programming language needed to use some libraries
openldap	Light weight Directory Access Protocol
glibmm24	C++ interface for GLib popular library

The program and execution were as follows:

```
1 rpmbuild --rebuild gtk+extra-2.1.1-24.src.rpm
2 rpmbuild --rebuild python-gtkextra2-1.1.0-23.src.rpm
3 rpmbuild --rebuild python-pyfits-2.2.2-2.src.rpm
```

Following this the dependencies were installed using `sudo rpm -i *.` Once the *HEADER* files were installed, the software was ready for use, however the nodes were not granted internet access for security reasons. To do this, an IP forwarding approach was used to allow only access to one link. This is a requirement for any analysis to be done with the Model++ software. Installing the software on the nodes was done as follows:

```
1 export CHROOT=/opt/ohpc/admin/images/centos7.5 #directory for
    compute nodes image
2 yum -y --installroot=$CHROOT install numpy cfitsio mariadb python
    python34 gsl gsl-devel fftw ruby openldap openldap-clients
    glibmm24
3 yum -y --installroot=$CHROOT install rpmbuild/RPMS/x86_64/*
4 sudo wwvnfs --chroot $CHROOT #build compute node images
5 sudo clush -w CN[00-06] reboot
```

Command 1 was to set the environment variable CHROOT to the compute node image path, 2–3 for installing the dependencies and libraries, 4-5 to build and reboot the compute nodes.

As mentioned in Subsection 4.2.1, the HPC has many users and not all users may be familiar with the changes that are required to use the software thus, before using the software, the environment needs to be set by running the following commands:

```
## remove gcc v 7 and python 3
export PATH=/opt/ohpc/pub/mpi/openmpi3-gnu7/3.1.0/bin:/opt/ohpc/pub/
    utils/prun/1.2:/opt/ohpc/pub/utils/autotools/bin:/opt/ohpc/pub/
    bin:/usr/local/bin:/usr/bin:/usr/local/sbin:/usr/sbin:/opt/pbs/
    bin:/home/jshapopi/bin
export LD_LIBRARY_PATH=/opt/ohpc/pub/mpi/openmpi3-gnu7/3.1.0/lib

# Set up ROOT
source /home/software/hess/root/root_v5.34.36/bin/thisroot.sh

# AstroROOT
export ISDC_ENV=/home/software/hess/root/astroroot
source $ISDC_ENV/bin/astroroot_init_env.sh

## H.E.S.S. Software
export HESSROOT=/home/software/hess/ParisAnalysis/HESS_Soft_0-8-34
export PATH=$HESSROOT/bin:$PATH
export LD_LIBRARY_PATH=$HESSROOT/lib:$LD_LIBRARY_PATH

# Environment variable names required by Model++
export PATH=$HESSROOT/scons/local:$PATH
alias scons="scons.py"
export SCONSFLAGS="--jobs=10"
```

All line sections have been commented for understanding.

B.1 *TChain* code

To build a TChain from multiple Micro-DSTs, the following code was used:

```
void EventList() {

string txt;    //text file with name of dst's
cout << "Please enter the name of the txt with Micro DST names" <<
    endl;
cin >> txt;

ifstream list(txt.c_str()); // read it in


string line;     //Name for each DST.
chain = new TChain("EventsNTuple");    //Create chain
while(getline(list, line)){      //Read in Micro-DST text file line
    by line
chain->AddFile(line.c_str());    //Add each line (EventList) to chain
}
EventsNTuple->StartViewer();
}
```

This code will ask for a text file with a list of all the names as stored on hard drive, of the Micro-DSTs and make a *TChain* with all of these attached. After all this, the *Tree Viewer* for visual representation of the Micro-DSTs is started.

Appendix C

Supplementary Plots for Cyg X-1 Cross-correlations

The hard state cross-correlations of X-rays in all three ASM bands, with 15 GHz radio data are left out of Subsection 5.4.1, as they do not exhibit any different features and are thus placed here. Figures C.1a, C.1b and C.1c all bear resemblance to the 1.5–12 keV plot in Figure 5.16a. Furthermore, their minute differences do not warrant or motivate an investigation into their features on a sub-daily level.

Figure C.2 contains all other correlations between the radio 15 GHz and different energy bands of MAXI and states of Cyg X-3 not presented in Subsection 5.4.1.

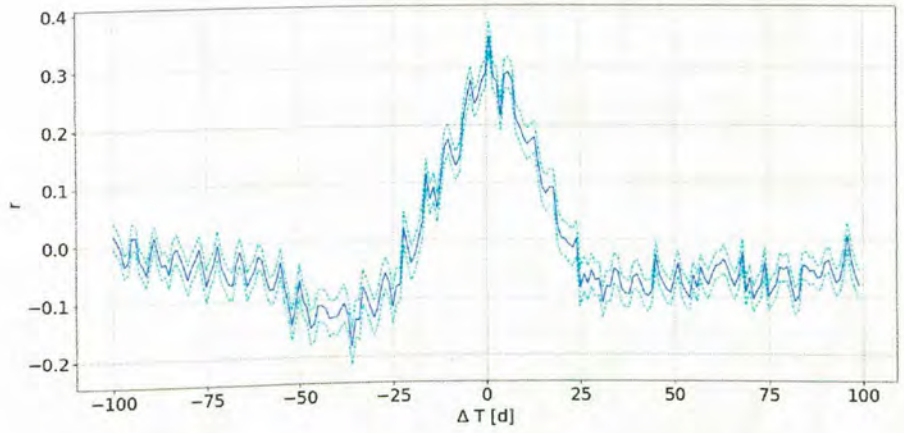

(a) 1.5–3 keV.

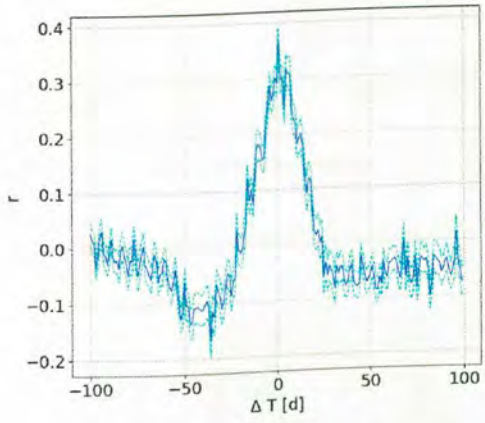

(b) 3–5 keV.

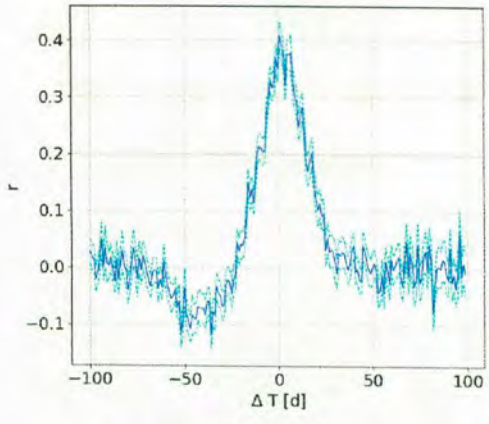

(c) 5–12 keV.

Figure C.1: Correlation of different energy bands of ASM data vs. 15 GHz radio data, in hard/intermediate state of Cyg X-1. In all plots, the blue is the correlation and cyan is its error. a), b) and c) are all similar in shape and peak height suggesting a uniform X-ray flux over the different energy bands in the hard/intermediate state.

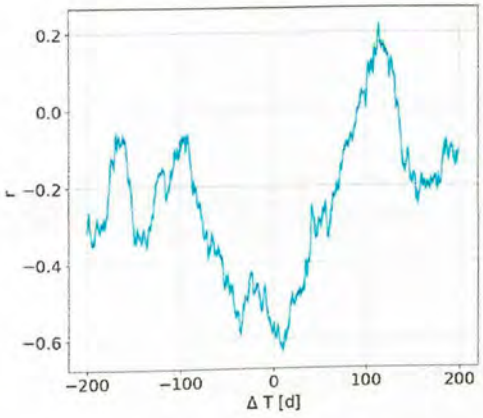

(a) 2 – 4 keV in all states

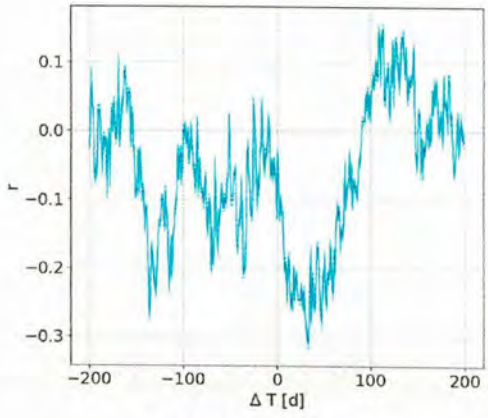

(b) 4 – 10 keV in all states

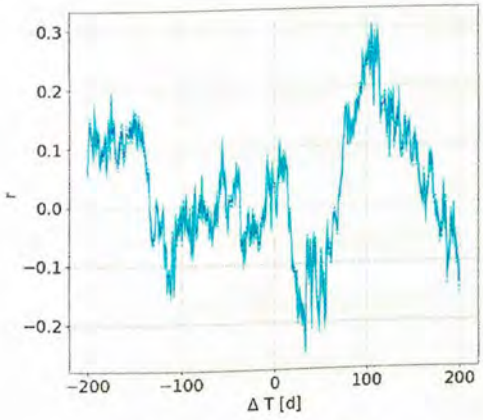

(c) 2 – 4 keV in hard state

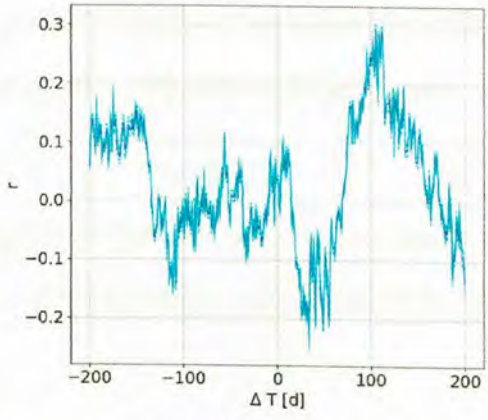

(d) 4 – 10 keV in hard state

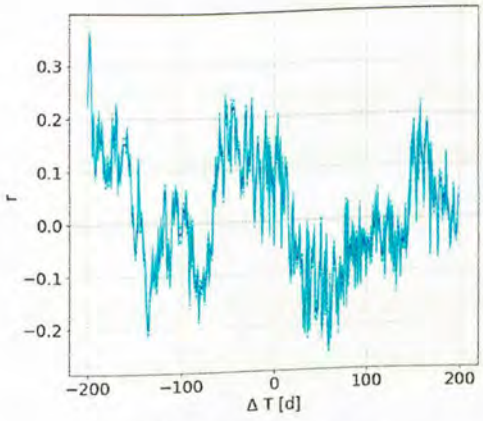

(e) 2 – 4 keV in soft state

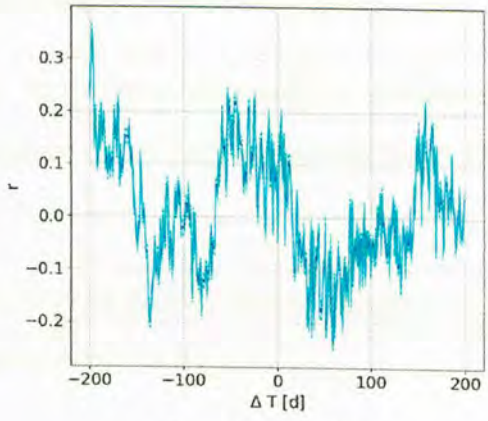

(f) 4 – 10 keV in soft state

Figure C.2: Results for cross-correlations of un-binned 15GHz with MAXI data in 2 – 4 keV range (a, c and e) and 4 – 10 keV range (b, d and f) in different states of Cyg X-1. The blue is the correlation and cyan is its error. A similar trend is seen in the different energy bands for the respective states. In a), the 2 – 4 keV energy band is strongly anti-correlated with the radio data while b) is also anti-correlated, however, weakly. c) and d) have no difference in shape or peak heights, i.e. there is a uniform X-ray flux in both energy bands. The same can be seen between e) and f), respectively.

Bibliography

[1] Abdalla H *et al.* (H.E.S.S. Collaboration) 2017 *Astronomy and Astrophysics* **600** A89

[2] Holler M *et al.* (H.E.S.S. collaboration) 2015 Observations of the Crab Nebula with H.E.S.S. Phase II *Proceedings of the 34th International Cosmic Ray Conference (ICRC2015)*

[3] Thaele J K 2016 *A comparitive study of a γ-Hadron seperation and analysis of Crab Nebula data measured by first G-APD Cherenkov Telescope* Ph.D. thesis TU Dortmund University

[4] Weekes T C 2003 *Very High Energy Gamma-Ray Astronomy* Series in Astronomy and Astrophysics (CRC Press) ISBN 9781420033199

[5] Bradt H 2004 *Astronomy Methods: A Physical Approach to Astronomical Observations* Cambridge Planetary Science (Cambridge University Press) ISBN 9780521535519

[6] Perkins D 2008 *Particle Astrophysics, Second Edition* Oxford Master Series in Physics (OUP Oxford) ISBN 9780199545452

[7] Wagner W 2004 *Design and Realisation of a new AMANDA Data Acquisition System with Transient Waveform Recorders* Ph.D. thesis TU Dortmund University

[8] Backes M 2011 *Long-term observations of the TeV blazar 1ES 1959+650* Ph.D. thesis TU Dortmund University

[9] Meyer M 2008 *Observations of a systematically selected sample of high frequency peaked BL Lac objects with the MAGIC telescope* Ph.D. thesis Julius Maximilian University of Würzburg

[10] Maoz D 2007 *Astrophysics in a Nutshell* In a Nutshell (Princeton University Press) ISBN 9780691125848

[11] Melia F 2009 *High-Energy Astrophysics* (Princeton) ISBN ISBN: 9780691140292

[12] Elert G The physics hypertextbook URL `https://physics.info/standard/`

[13] Oerter R 2006 *The Theory of Almost Everything: The Standard Model, the Unsung Triumph of Modern Physics* (Penguin Group) ISBN 978-0-13-236678-6

[14] Griffiths D 2008 *Introduction to Elementary Particles* Physics textbook (Wiley) ISBN 9783527406012

[15] Jain P and Sharma L 1998 *Journal of Applied Science in Southern Africa* **4** 80–101

[16] Weinberg S 1967 *Phys. Rev. Lett.* **19**(21) 1264–1266

[17] Urry C M and Padovani P 1995 *Publications of the Astronomical Society of the Pacific* **107** 803–841

[18] Saxton B A unified AGN model URL `https://public.nrao.edu/gallery/a-unified-agn-model`

[19] Singh K P 2013 *Bulletin of the Astronomical Society of India* **41** 137

[20] Sambruna R M 1997 *The Astrophysical Journal* **487** 536–554

[21] Duchêne G and Kraus A 2013 *Annual Review of Astronomy and Astrophysics* **51** 269–310

[22] Shakura N I and Sunyaev R A 1973 *Astronomy and Astrophysics* **24** 337

[23] El Mellah, I, Sundqvist, J O and Keppens, R 2019 *Astronomy and Astrophysics* **622** L3

[24] Lamers H J G L M, van den Heuvel E P J and Petterson J A 1976 *Astronomy and Astrophysics* **49** 327–335

[25] Oskinova L M, Feldmeier A and Kretschmar P 2012 *Monthly Notices of the Royal Astronomical Society* **421** 2820–2831 ISSN 0035-8711

[26] Stevens I R 1988 *Monthly Notices of the Royal Astronomical Society* **232** 199–213 ISSN 0035-8711

[27] Shapiro S L and Lightman A P 1976 *Astrophysical Journal* **204** 555–560

[28] Savonije G J 1979 *Astronomy and Astrophysics* **71** 352–358

[29] van den Heuvel E P J 1975 *Astrophysical Journal* **198** L109–L112

[30] Fryer C L 1999 *The Astrophysical Journal* **522** 413–418

[31] Mirabel I F and Rodríguez L F 1998 *Nature* **392** 673–676 ISSN 1476-4687

[32] Bowyer S, Byram E T, Chubb T A and Friedman H 1965 Observational results of X-ray astronomy *Astronomical Observations from Space Vehicles (IAU Symposium* vol 23) ed Steinberg J L p 227

[33] A Zdziarski A, Skinner G, Pooley G and Lubinski P 2011 *Monthly Notices of The Royal Astronomical Society* **416** 1324–1339 ISSN 0035-8711

[34] Orosz J A, McClintock J E, Aufdenberg J P, Remillard R A, Reid M J, Narayan R and Gou L 2011 *Astrophysical Journal* **742** 84 (*Preprint* 1106.3689)

[35] Mastroserio G, Ingram A and van der Klis M 2019 *Monthly Notices of the Royal Astronomical Society* **488** 348–361 (*Preprint* 1906.08266)

[36] Sota A, Apellániz J M, Walborn N R, Alfaro E J, Barbá R H, Morrell N I, Gamen R C and Arias J I 2011 *The Astrophysical Journal Supplement Series* **193** 24

[37] Gies D R and Bolton C T 1986 *Astrophysical Journal* **304** 371

[38] Zdziarski A A, Malyshev D, Chernyakova M and Pooley G G 2017 *Monthly Notices of the Royal Astronomical Society* **471** 3657–3667

[39] GIS Geography 2019 Why the atmospheric window matters in earth science URL `https://gisgeography.com/atmospheric-window/`

[40] Winkler C *et al.* 2003 *Astronomy & Astrophysics* **411** L1–L6

[41] Atwood W B *et al.* 2009 *The Astrophysical Journal* **697**

[42] Barthelmy S D *et al.* 2005 *Space Science Reviews* **120** 143–164 ISSN 1572-9672

[43] Sinnis G 2009 *New Journal of Physics* **11** 055007

[44] Amenomori M *et al.* 2011 *Astrophysics and Space Sciences Transactions* **7** 15–20

[45] Aharonian F *et al.* (H.E.S.S. Collaboration) 2006 *Astronomy and Astrophysics* **457** 899–915

[46] Hinton J 2009 *New Journal of Physics* **11** 055005

[47] Moiseev A *et al.* 2007 *Astroparticle Physics* **27** 339 – 358 ISSN 0927-6505

[48] Myers J Overview of the LAT URL `https://fermi.gsfc.nasa.gov/ssc/data/analysis/documentation/Cicerone/Cicerone_Introduction/LAT_overview.html`

[49] Zdziarski A A *et al.* 2018 *Monthly Notices of the Royal Astronomical Society* **479** 4399–4415 ISSN 0035-8711

[50] Kneissl R *et al.* 2001 *Monthly Notices of the Royal Astronomical Society* **328** 783–794 ISSN 0035-8711

[51] Zwart J T L *et al.* 2008 *Monthly Notices of the Royal Astronomical Society* **391** 1545–1558 ISSN 0035-8711

[52] Levine A M *et al.* 1996 *The Astrophysical Journal* **469** L33–L36

[53] Matsuoka M *et al.* 2009 *Publications of the Astronomical Society of Japan* **61** 999–1010 ISSN 0004-6264

[54] de Naurois M and Rolland L 2009 *Astroparticle Physics* **32** 231 – 252

[55] Hillas A M 1985 Cerenkov light images of EAS produced by primary gamma rays and by nuclei *Proceedings of the 19th International Cosmic Ray Conference*

[56] Alexander T 1997 *Is AGN Variability Correlated with Other AGN Properties? ZDCF Analysis of Small Samples of Sparse Light Curves* (*Astrophysics and Space Science Library* vol 218) p 163

[57] Robertson D R S, Gallo L C, Zoghbi A and Fabian A C 2015 *Monthly Notices of the Royal Astronomical Society* **453** 3455–3460

[58] Edelson R A and Krolik J H 1988 *Astrophysical Journal* **333** 646–659

[59] Bernet R Standard model URL `https://www.physik.uzh.ch/en/researcharea/lhcb/outreach/StandardModel.html`